

## Article

# The Contribution of Near-Surface Geophysics for the Site Characterization of Seismological Stations

John D. Alexopoulos , Spyridon Dilalos \* , Nicholas Voulgaris, Vasileios Gkosios, Ioannis-Konstantinos Giannopoulos, Vasilis Kapetanidis  and George Kaviris 

Department of Geology and Geoenvironment, Section of Geophysics and Geothermy, National and Kapodistrian University of Athens, Panepistimioupoli Zografou, 15784 Athens, Greece; jalexopoulos@geol.uoa.gr (J.D.A.); voulgaris@geol.uoa.gr (N.V.); vgnosios@geol.uoa.gr (V.G.); jkgianno@geol.uoa.gr (I.-K.G.); vkapetan@geol.uoa.gr (V.K.); gkaviris@geol.uoa.gr (G.K.)

\* Correspondence: sdilalos@geol.uoa.gr

**Abstract:** The Athenet network is the network of the Seismological Laboratory of the National and Kapodistrian University of Athens. We present the geophysical investigation that has been carried out at six seismological stations of the Athenet network for their site characterization. More specifically, at the location of each seismological station, four geophysical methods have been carried out: Seismic Refraction Tomography (SRT), Multichannel Analysis of Surface Waves (MASW), the Horizontal to Vertical Spectral Ratio (HVSr) technique, and Electrical Resistivity Tomography (ERT). The applied geophysical survey provided important information regarding the site characterization at the selected seismological stations, including key parameters such as the fundamental frequency  $f_0$ , the shear-wave velocity  $V_S$ , the average shear-wave velocity for the upper 30 m depth ( $V_{S30}$ ), the seismic bedrock depth, the soil type, and the subsurface geology. Moreover, selected elastic moduli (Poisson's ratio, shear, bulk, and Young moduli) have been calculated. The site characterization information contributes to the determination of the amplification factors for each site that can lead to more accurate calculation of Peak Ground Acceleration (PGA) or Peak Ground Velocity (PGV) and, therefore, trustworthy Probabilistic and Stochastic Seismic Hazard Assessments. The derived fundamental frequency for the seismological stations of *VILL*, *LOUT*, *THAL*, and *EPID* have been determined to be equal to 10.4, 2.7, 1.4, and 7.1 Hz and their amplification factors to be 1.9, 3.1, 1.7, and 2.6, respectively. For stations *MDRA* and *ATAL*, these parameters could not be determined.

**Keywords:** SRT; MASW; ERT; HVSr; elastic moduli;  $V_{S30}$ ; EC8



**Citation:** Alexopoulos, J.D.; Dilalos, S.; Voulgaris, N.; Gkosios, V.; Giannopoulos, I.-K.; Kapetanidis, V.; Kaviris, G. The Contribution of Near-Surface Geophysics for the Site Characterization of Seismological Stations. *Appl. Sci.* **2023**, *13*, 4932. <https://doi.org/10.3390/app13084932>

Academic Editors: Javier Elez and Jorge L. Giner-Robles

Received: 27 March 2023

Revised: 11 April 2023

Accepted: 13 April 2023

Published: 14 April 2023



**Copyright:** © 2023 by the authors. Licensee MDPI, Basel, Switzerland. This article is an open access article distributed under the terms and conditions of the Creative Commons Attribution (CC BY) license (<https://creativecommons.org/licenses/by/4.0/>).

## 1. Introduction

The permanent network of the Seismological Laboratory of the National and Kapodistrian University of Athens is the Athenet network (SL-NKUA), and its code is HA [1]. It currently comprises 24 weak- and 7 strong-motion sensors, operating in real-time. The stations are mainly deployed in Central Greece, covering the Gulf of Corinth, Euboea Island, and, partly, Saronikos Gulf (Figure 1). All seismological stations of the Athenet network transmit data to the central server of SL-NKUA in real-time, at a sampling rate of 100 sps, through 4G or GPRS telemetry. Since June 2008, SL-NKUA has been one of the institutes that contribute to the Hellenic Unified Seismological Network (HUSN) [2]. HUSN is a virtual network of seismological and accelerometric stations, which has unified the individual networks of different institutes in Greece, namely the Geodynamic Institute of the National Observatory of Athens [3], the Department of Geophysics of the Aristotle University of Thessaloniki [4], the Seismological Laboratory of the University of Patras [5], the Hellenic Mediterranean University Research Center [6], and the Institute of Engineering Seismology and Earthquake Engineering [7]. Waveform data are shared between the partners of HUSN in real-time and are also freely available to the public through the European Integrated Data Archive (EIDA), hosted at GI-NOA [2].

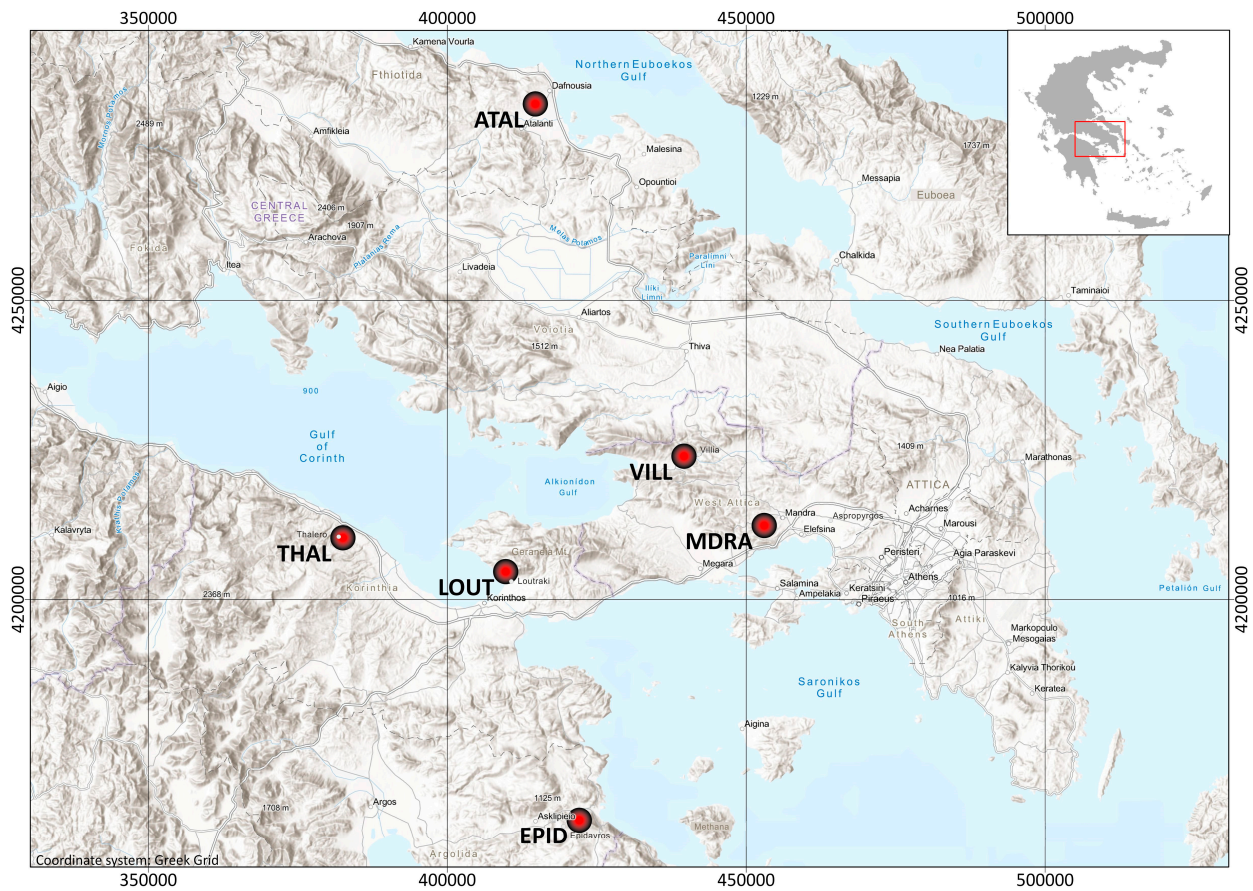


**Figure 1.** Locations of the investigated areas and selected seismological stations (red circles).

The past few years have witnessed a significant rise in the number of permanent seismic network stations globally. This increase has resulted in a surge of earthquake recordings and their real-time data applications. The availability of vast seismic datasets has brought to the forefront the intricate nature of ground-motion prediction and its direct correlation to the characteristics of the site where the recording instrument was installed.

The local subsurface characteristics have significant impact on surface ground motions, and their determination is beneficial in seismological studies. For example, they are usually determined in the context of seismic hazard assessment [8,9], estimation of Ground Motion Prediction Models (GMPMs) [10,11], and classification of soil for microzonation studies [12]. For that reason, the identification of the peak frequencies which exhibit significant amplification is crucial.

In this paper, we present the geophysical investigation that has been carried out at selected seismological stations of the Athenet network (Figure 1) in order to calculate essential parameters for their site characterization. For that reason, we applied a multidisciplinary geophysical survey, including the Horizontal to Vertical Spectral Ratio (HVSr) technique, Seismic Refraction and Multichannel Analysis of Surface Waves (MASW) measurements [13–18], and Electrical Resistivity Tomography (ERT) measurements, near the selected stations (Figure 1). These methods are fast, reliable, and have been used in several similar cases for the site characterization of seismological stations in the past [19–23]. Compared to geotechnical methods, which involve collecting data from boreholes, the geophysical methods are of significantly lower cost and, therefore, are often the preferred choice.

Credible site characterization for a seismic station requires the determination of several key parameters. According to [19], the most important ones are the fundamental frequency ( $f_0$ ), shear-wave velocity distribution ( $V_s$ ), average shear-wave velocity in the upper 30

m of the site ( $V_{S30}$ ), depth of seismic ( $H_{seis}$ ) bedrock, surface geology, and soil-type classification at each site. These parameters are crucial in estimating the potential effects that can be induced in the seismic recordings, such as distortion of the amplitude, frequency spectrum, and duration of the signal. Therefore, a thorough understating of these parameters is essential in ensuring accurate and reliable seismic data analysis, with precise and dependable results.

## 2. Methodology

In total, six seismic and electrical sections were carried out for the site characterization of each seismological station. The acquisition of all geophysical data was accomplished during the summer of 2021. The Seismic Refraction Tomography (SRT) and Electrical Resistivity Tomography (ERT) methods were basically chosen for the determination of the subsurface geology of each seismological station. The HVSR method was selected for the calculation of the fundamental frequency ( $f_0$ ) and the corresponding depth of the seismic bedrock. Finally, the application of MASW provided the  $V_S$  distribution,  $V_{S30}$ , and therefore the soil-type classification.

### 2.1. Seismic Method

The HVSR technique [24] is a widely used method to assess the effects of local ground conditions on seismic wave amplification. It is based on the ratio between horizontal ( $H$ ) to vertical ( $V$ ) components of ground motion. By calculating the HVSR, the fundamental frequency and the corresponding amplification factor of the ground motion can be estimated. To apply the HVSR technique, ground ambient noise recordings, or microtremors, need to be collected. This method enables the rapid and efficient evaluation of the impact of local ground conditions on seismic wave amplification, making it an important tool in earthquake engineering. The HVSR technique has been previously applied successfully in many studies worldwide [25–31] as well as in Greece [32–36].

The HVSR technique is based on the fundamental assumption that on hard ground (rock) both vertical and horizontal components of ground motion exhibit similar amplification during seismic excitation, whereas on soft soil the horizontal components are strongly influenced by the response of the surface geological formations. Thus, the H/V ratio of the microtremors can be used to determine the fundamental frequency ( $f_0$ ) and the corresponding soil amplification factor ( $A_0$ ) of the surface layers at each location. For this technique, it is necessary to calculate the H/V spectral ratio from the continuous recording of the background ground noise.

The Shallow Seismic Refraction (SSR) technique is commonly used in similar investigations [37–39]. It is considered to be one of the primary geophysical methods for the investigation of the subsurface lithological structure. Through the propagation of the elastic waves, their velocities in soil deposits and rocks can be determined and the corresponding elastic moduli can also be calculated [15–18]. Depending on the applied technique used for the data processing, the subsurface structure can be represented either as a discrete layered model, with constant seismic velocities, or as a gridded model with gradient velocity variations, capable of adumbrating lateral heterogeneities. The discrete layered model can be obtained by the application of conventional techniques (e.g., time-term inversion, GRM), while the gridded model can be obtained by a tomographic inversion approach, widely known as SRT. The SRT technique has the benefit of producing more accurate and high-resolution velocity models, whereas the extensive amount of fieldwork and the increased processing time needed are some of the downsides [38]. Through this technique, the recorded seismic refraction data can be inverted, and the distribution of the seismic wave velocities can be obtained across two-dimensional (2D) sections, which are widely affected by the physical properties of the subsurface [40–44].

The MASW technique is a non-invasive seismic method which has been widely used for soil characterization purposes [45–47]. It is implemented to obtain shear-wave velocities in shallow geophysical investigations, derived by analyzing the surface wave (Rayleigh)

components on the seismic recordings. The MASW technique has the advantages of lower fieldwork costs and easier recording and processing. It is known for its effectiveness and reliability in providing shear-wave velocity profiles within the first 30 m of the subsurface [45,46,48–51]. It is acknowledged that P- and S-wave velocities provide useful context regarding the liquefaction potential, ground motion, and natural frequency function in case of an earthquake. Hence, considerable knowledge of soil stiffness is a key parameter for more accurate prediction of ground response and amplification estimation.

#### 2.1.1. Data

The field measurements of seismic refraction and MASW data were acquired by a 24-channel Geometrics SmartSeis seismograph, with a sampling interval of 0.250 ms and a total record length of 512 ms. A total of 24 vertical geophones, evenly spaced at 1.0 m along each seismic line (Figure A1), were used for the detection of the seismic waves. Two types of geophones with natural frequencies of 4.5 and 10.0 Hz were used in order to enhance the recording of surface and body waves, respectively. The seismic energy was generated by a 6 kg sledgehammer that was impacted on a metallic plate for better transmission of the energy to the ground. For the 1D MASW technique, the active receiver spread length was 23 m, with a near offset of 4 m at both ends of the seismic line (Figure A1). Moreover, we acquired measurements at variable near offsets (4–6 m) to record different wavelengths of the surface (Rayleigh) waves and expand the sampling depth. Regarding the SRT technique, multiple seismic recordings were acquired by nine different shot locations, placed at both ends and in between the spread length, with 2.5 to 3.0 m spacing (Figure A1). Furthermore, two outshots were performed at a distance of 10 m from both ends of the seismic array (Figure A1) to record the arrival times of the critically refracted wave through the entire length of the spread. At each shot location, three to five stacks were implemented to suppress the unwanted noise and increase the signal-to-noise ratio (SNR). Regarding the HSVR technique, the dataset consists of continuous three-component microtremor recordings, with a duration of at least 30 min. This dataset needs to be processed in several distinct time windows of about 30 s each, from which an average spectral ratio and the corresponding standard deviation at each frequency will be obtained.

#### 2.1.2. Processing

##### HVSR Technique

In the present study, we employed the *GEOPSY* software, which was developed within the framework of the European Research Project SESAME/2003-2007 [52]. This software provides important parameterization capabilities concerning window selection and smoothing filters. The input signal is the background ground noise, i.e., the ground motion caused by distant excitations and waves arriving at the recording site after being scattered, particularly within a volume around the site, thus providing a type of sampling of the subsurface of the recording area. Therefore, various environmental or local anthropogenic noises, such as wind, footsteps close to the recording instrument, passing cars, etc., or even an earthquake, are unwanted noises that could pose a problem in the application of the HVSR technique with ambient noise data.

For that reason, the *GEOPSY* software provides the possibility of using “anti-triggering” filters, employing the classical Short-term Average to Long-term Average “STA/LTA” technique [53] used in seismology to detect the arrival of seismic waves by estimating the “Signal-to-Noise Ratio” (SNR). A sharp increase in SNR to values above a threshold, usually 2.0–3.0, is an indication that an impulsive signal of high amplitude is entering the window under consideration. In the application of the HVSR technique, the arrival of a strong “signal” is an indication that the following window contains unwanted “noise”, and thus should be rejected (anti-triggering).

In the *GEOPSY* software, both the length of the STA and LTA windows and the minimum and maximum STA/LTA ratios (Figure 2) can be configured to determine whether a specific window is used or not. For the present study, which explores the site effects at

the locations of permanent seismological stations, we used 6 h long recordings during the relatively quiet hours of the night to early morning to study the HVSR of microtremors. The recordings were detrended, and a high-pass Butterworth filter with a corner frequency of 0.1 Hz was applied in the original recordings to remove long-period noise. After testing windows of various lengths, we chose to apply measurements in 60 s long windows, with a 5% overlap permitted for consecutive ones. This achieves smoother results than the 30 s window and is small enough to permit a large number of different windows. An STA/LTA anti-triggering filter was applied to both the raw waveform and a 5.0 Hz high-pass filtered version to detect earthquakes or other instances of unwanted transient noise. An average of around 100 windows with the least amount of transient noise was selected at each station for the application of the HVSR method.

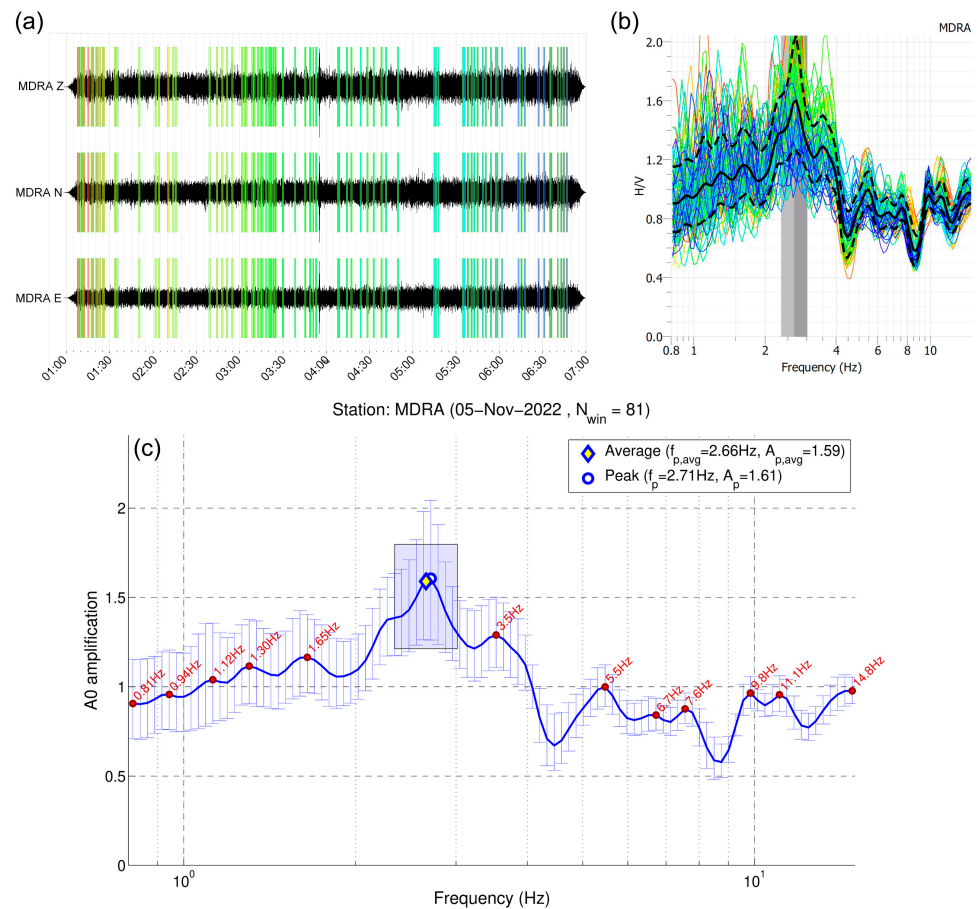


**Figure 2.** Example from the construction of HVSR curves, for the recordings of station MDRA on 5 November 2022. (a) Selection of 81 windows of 60 s length each (vertical colored rectangles) from 6 h continuous records using STA/LTA anti-trigger criteria; (b) individual HVSR spectra, with the color of each line corresponding to the colors of the respective windows in panel (a), average spectra (solid black line), and respective errors (dashed black lines). The vertical light and dark gray bands indicate the frequency bands corresponding to the dominant peak frequency,  $f_p$ ; (c) a simplified figure of the average HVSR curve (bold blue line), including error bars for each frequency (vertical thin blue lines). The semi-transparent rectangle corresponds to the frequency range depicted by the light and dark gray vertical bands in panel (b), with its height corresponding to the average minimum and maximum amplifications for this specific frequency range, with the average frequency depicted by a yellow (with blue outline) diamond symbol. The blue circle indicates the global peak frequency of the average HVSR spectrum. The red circles mark the local maxima of the HVSR curve, corresponding to secondary peaks, with the frequencies labeled with red text.

Then, for each of the selected windows, a Fast Fourier Transform is applied to each component to obtain the respective spectra. The processing includes the application of a 5% Tukey taper window and a Konno–Ohmachi [54] smoothing window, with a 15% width on a logarithmic scale. The geometric mean of the two horizontal components is calculated to obtain an average spectrum, as recommended by the SESAME guidelines [52]. Finally, the HVSR is calculated for each individual window. From the distribution of spectral ratios for each selected window, the average spectral ratio and standard deviation at each frequency are calculated. *GEOPSY* automatically determines a band containing the dominant peak frequency, with the maximum corresponding ground amplification factor. The determined dominant frequency peak is practically the fundamental resonant frequency,  $f_0$ , and its associated amplification factor,  $A_0$ . An example of the microtremor processing with *GEOPSY* at station MDRA is presented in Figure 2. It is noted that tests using the squared average of the horizontal components usually resulted in slightly higher amplification factor values.

To avoid cases where the ambient noise conditions on a specific day were biased due to a local noise source or lack of energy in certain frequency bands, the HVSR measurements at each site were repeated for recordings of different days. The results were then evaluated on a day-specific level but also collectively, also taking into account possible changes in a station's instrumentation. Moreover, the variations of the fundamental frequency for the same station may be due to the nature of the acquired data. We also focus on secondary peak frequencies of the HVSR, to distinguish the possible fundamental frequency, as well as other peaks likely associated with different geological layers.

### SRT Technique

The seismic refraction data processing was carried out using the *SeisImager/2D* software package provided by *Geometrics Inc.* (San Jose, CA, USA). Using the *Pickwin* module of the software, six group file lists were created, containing every seismic record (11 in total) that was acquired at each measurement site (Figure A1). For each file list, the shot locations, the first receiver location, and the spacing between the receivers were defined. After the assignment of the geometric characteristics of the arrays, the first break arrivals of the P-waves were picked for every seismic record. Afterwards, the picked arrival times of the P-waves were plotted as a function of the distance between the receivers, to construct the traveltimes–distance curves for each measurement site. These curves were edited using the *Plotrefa* module of the software, where some arrival times were corrected and the traveltimes reciprocity between opposite shots was verified.

Two methods, provided by *Plotrefa*, were used to analyze the seismic refraction data. First, the time-term inversion method was implemented, where the first break arrival times are inverted through linear least-squares and delay time analysis for the generation of a seismic velocity section [55]. To start the inversion process, each arrival time (direct or refracted) of the traveltimes–distance curves was assigned to a specific layer, and the topography of the seismic line was also defined. After the inversion procedure, a 2D layered velocity model was created with distinct boundaries between the layers and a constant velocity value at each layer. The obtained velocity model was used as the starting initial model for the application of the SRT method. Therefore, the velocity model was converted into a grid model with a constant velocity value assigned at each cell. The software employs the wavefront propagation method for forward modelling, where the synthetic traveltimes curves, corresponding to the initial model, are generated. Subsequently, the synthetic traveltimes curves are compared with the observed traveltimes curves, and through the application of the nonlinear least-squares approach [40,55], the velocity model is updated in order to reduce the misfit error between the two traveltimes curve sets. This procedure is repeated until the minimum possible RMS error is achieved within a predefined number of iterations. The outcome of the application of the SRT technique was a 2D P-wave velocity distribution to the subsurface in the direction of the seismic line. The RMS error for all the SRT sections was below 1.0 ms, providing high reliability of the results.

## MASW Processing

The MASW technique is based on the propagation characteristics of surface waves, and especially the Rayleigh, which travel with different propagation velocities (phase velocities) at different frequencies throughout a heterogeneous medium. As a result, the low-frequency components of the surface waves penetrate deeper into the subsurface and are mainly affected by the elastic properties of the deeper layers [56]. On the other hand, the high-frequency components are constrained to the shallow subsurface zone and contain information about the shallow layers. This dispersive property is utilized to construct the dispersion curve, which is the phase velocity vs. frequency plot. By applying a mathematical inversion to the dispersion curve, the distribution of the S-wave velocity through the subsurface can be calculated.

MASW data processing was carried out using the *SeisImager/SW* software package provided by Geometrics Inc. The acquired seismic records were first processed using the *Pickwin* module, to improve their quality and assign the geometry of the seismic experiment. For that reason, frequency filters were applied in order to reduce the influence of the recorded body waves and the unwanted noise, while the geophone spacing and the *near-offset* distance were defined for each seismic record. Furthermore, the *phase shift* method [47] was implemented to construct the dispersion image for each record. This method uses a *Fast Fourier Transformation* to convert the acquired seismic records from the time domain to the frequency domain, while it also calculates the *phase velocities* of the Rayleigh waves.

Each multichannel seismic record was converted to the frequency domain, and their corresponding dispersion curves were generated by picking the maximum energy amplitude at the frequency range of 4.5–50.0 Hz. Afterwards, with the contribution of the *WaveEq* module, a bandpass filter was applied to the dispersion curves to remove the noisy picks. To invert the dispersion curve, a theoretical initial velocity model was created with the depth conversion result method, which was incorporated by the software. This method estimates the  $V_s$  values by multiplying the phase velocities with a factor equal to 1.1, while it uses the one-third wavelength approximation in order to estimate the depth. The minimum and maximum phase velocity values are defined by the highest and lowest frequency peaks in the dispersion curves, correspondingly. Subsequently, the least-squares method was used to run the inversion process. The initial model was modified five times for the calculated dispersion curve to best match the observed data. Finally, the 1D shear-wave velocity model was calculated, which corresponded to the midpoint of the seismic line.

The  $V_{S30}$  value refers to the time–depth averaged shear-wave velocity of the top 30 m of a layered subsurface, and it is calculated by the following equation [57]:

$$V_{s30} = \frac{30}{\sum_{i=1}^N \frac{h_i}{V_i}} \quad (1)$$

where  $V_i$  and  $h_i$  are the shear-wave velocity and thickness of the  $i$ th layer, in a total number of  $N$  layers, of the top 30.0 m of the propagation medium.

According to the European Committee for Standardization Eurocode 8 [57], the  $V_{S30}$  is used for the classification of the ground type, as shown in Table 1.

## 2.2. Electrical Resistivity Tomography

ERT investigates the horizontal and vertical distribution of the subsurface resistivity and is widely used for near-surface applications, geotechnical investigations, and lithological variations [58–60]. It can adumbrate the existence of subsurface discontinuities, fractures, or even voids. It is generally accepted that the ERT technique is more sensitive to variations in the subsurface soil properties than other geophysical techniques. ERT is well known for its high-resolution subsurface investigation, which is basically defined by the geometry of the electrodes used for the data acquisition. The processing results are a 2D image of the subsurface resistivity distribution.

**Table 1.** Ground-type classification based on [57].

Ground Type	Description of Stratigraphic Profile	$V_{S30}$ (m/s)
A	Rock or other rock-like geological formations, including at most 5 m of weaker material at the surface.	>800
B	Deposits of very dense sand, gravel, or very stiff clay, at least several tens of meters in thickness, characterized by a gradual increase of mechanical properties with depth.	360–800
C	Deep deposits of dense or medium-dense sand, gravel, or stiff clay with thickness from several tens to many hundreds of meters.	180–360
D	Deposits of loose-to-medium cohesionless soil (with or without some soft cohesive layers), or of predominantly soft-to-firm cohesive soil.	<180

In the present study, the Wenner array was applied, using a minimum electrode spacing of 1 m, for the determination of the near-surface resistivity distribution in the chosen seismological stations. The depth of investigation was adequate for the purpose of the study. The ABEM geoelectrical system was used.

The *Res2DInv* Software by *Geotomo* was used for the processing of the acquired resistivity data. During this processing, the software develops an initial model and tries to minimize the misfit error between this model and the raw data points. The inversion process continues until the minimum possible misfit error is achieved. At first, the quality of the acquired data was checked, by removing any possible bad points that would also affect the inversion process. Afterwards, the inversion was carried out based on the least-squares routine, since no extremely sharp boundaries were expected. In the inversion process, the topography of each section has also been embedded, since some of the stations had a smooth topographic relief.

For the estimation of the coordinates of each electrode and the topography of each geoelectrical line, we used dual-frequency *TopCon HiperPro GPS* antennas with Differential Global Positioning System (*dGPS*). The coordinate system used for this study was the local (Greek) EGSA'87 (Datum GGRS'80).

### 2.3. Density Determination

The determination of the density of geological samples based on laboratory measurements is proposed by several authors [61–66]. A typical procedure to achieve this task involves the measurement of three different types of weight for each specimen, i.e., (i) the dry weight of the specimen measured in air ( $W_1$ ), (ii) the saturated weight of the specimen measured in air ( $W_2$ ), and, finally, (iii) the saturated weight of the specimen measured while submerged in water. From this procedure, the dry bulk density  $\rho_d$ , the saturated bulk density  $\rho_s$ , and the granular density  $\rho_g$  can be obtained. In the context of this study, the physical properties of the subsurface are determined above the assumed level of the water table and, therefore, the use of the dry bulk density was considered to be more appropriate.

For the determination of the measurement error, the weights of several samples of each geological formation were measured (Table 2), taking into consideration their median characteristic value. In total, laboratory density measurements on 60 geological specimens, collected from the locations of the geophysical measurements, were performed. For more reliable results, a *Kern EMB 100-3* precision scale was used with an accuracy of 0.001 gr. In Table 2, the calculated densities of the geological formations from the three seismological stations (*MDRA*, *VILL*, and *ATAL*) are provided. Due to the existence of loose geological formations at the other sites of the seismological stations, i.e., *Loutraki*, *Thalero*, and *Epidavros* (*LOUT*, *THAL*, and *EPID*), the collection of a solid specimen and consequently the determination of the density was not possible. Therefore, the required density values for the ongoing calculations of the elastic moduli for those sites are based on literature sources [62,63,67].

**Table 2.** Density values of the geological formations of the investigated areas. The density values marked with an asterisk were obtained from the indicated literature (brackets).

Seismological Station	Geological Formation	Number of Specimens	Dry Density (gr/cm <sup>3</sup> )	Saturated Density (gr/cm <sup>3</sup> )	Standard Deviation
<i>MDRA</i>	Dolostones, dolomitic limestones, and limestones (TRm)	20	2.69	2.69	0.02
<i>VILL</i>	Dolostones, dolomitic limestones, and limestones (TRm)	20	2.66	2.67	0.03
<i>LOUT</i>	Talus and scree cones	-	2.3 * [62,63]	-	0.10
<i>THAL</i>	Marine-brackish marls (Pl-Pt.m)	-	1.72 * [62,63]	-	0.07
<i>ATAL</i>	Limestones and dolomites (Ji-m kD)	20	2.81	2.82	0.01
<i>EPID</i>	Trachytes and trachytic tuffs ( $\tau$ , tf)	-	2.04 * [67]	-	-

### 3. Application of the Geophysical Surveys and Processing Results

Herein, we provide a brief overview of the technical characteristics of each of the six seismological stations, along with a description of the local geological setting. These stations have been selected in order to test this combined geophysical methodology and its results, due to their different geological settings and the fact that they are close to Athens. Afterwards, we provide the processed geophysical data for each station and their findings.

#### 3.1. Seismological Station at Mandra, Attica (MDRA)

Station *MDRA*, located at the monastery of Panagia Gorgoepikoou (Figure 3), in the vicinity of Mandra town, western Attica, was deployed on 22 September 2020. *MDRA* station is currently equipped with a *GEObit GEOsix*, six-channel datalogger, and an R-sensors CME-6111, 60 s broadband seismometer. According to [68], the station (Figure 3) is based on dolostones, dolomitic limestones, and limestones of the Upper Triassic (*TRm*) of the Sub-Pelagonian Unit. Overlying them, limestones of the Upper Cretaceous (*Ks*) can be found, while in places, in the contact between the two carbonate formations, the development of lateritic bauxite ores can be observed.

The HVSr for station *MDRA* (Figure 4) exhibits a double peak at frequencies 2.3 and 2.7 Hz, with an amplification factor  $A \approx 1.7 \pm 0.3$ . However, a lower secondary frequency can be observed in some cases at  $f \approx 1.6$  Hz, with  $A \approx 1.4 \pm 0.3$ . Additionally, one more peak, at almost 0.9 Hz, is present in some records, but it is not very prominent. At frequencies greater than 5.5 Hz, the base level of amplification is around unity.

The results of the geophysical measurements carried out on the Triassic dolostones formation (*TRm*), at the *MDRA* seismological station, are presented in Figure 5. The SRT technique revealed three seismic layers with velocities:  $V_{P1} = 1500$  m/s,  $V_{P2} = 2000$  m/s, and  $V_{P3} > 2700$  m/s. The thicknesses of the first and second layers are relatively small, about 1.0 m each, while at depths greater than 2.0 m the seismic bedrock is located. Regarding the MASW technique results, the 1D model (Figure 5), due to the small thickness of the two first layers, revealed only one seismic layer with  $V_S = 1860$  m/s, which is considered to be the velocity of the seismic bedrock. The average shear-wave velocity of the first thirty meters of the subsurface was determined to be 1877 m/s. In Figure 5, the resistivity model from the ERT technique is also presented. The resistivity value of the solid bedrock, which in this case is Triassic dolostone, is considered to be greater than 9000 Ohm.m and is present below 2.0 m depth at the middle to the end of the ERT section.



**Figure 3.** Location of the seismological station *MDRA* and the geophysical measurements along with the geology of the area.

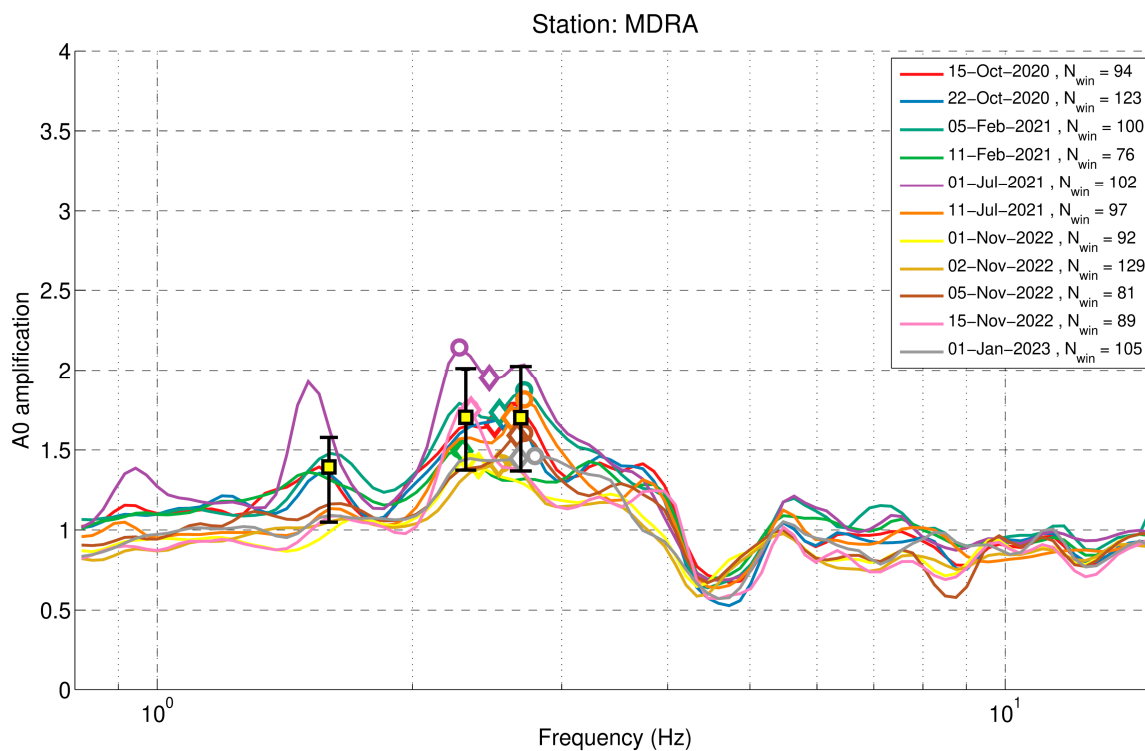


**Figure 4.** Average HVSR curves (solid lines) determined for station *MDRA* on different days, from 60 s long windows selected after the application of STA/LTA anti-triggering on 6 h long records. Circles denote the global frequency on each curve, while diamond symbols mark the average of the frequency band denoting the range of peak frequencies of the HVSR lines from the individually selected windows (light/dark gray band in Figure 2b). Squares mark the prominent global and secondary peak frequencies recognized from the HVSR spectra, with error bars indicating the uncertainty of the amplification factor (Table A1).

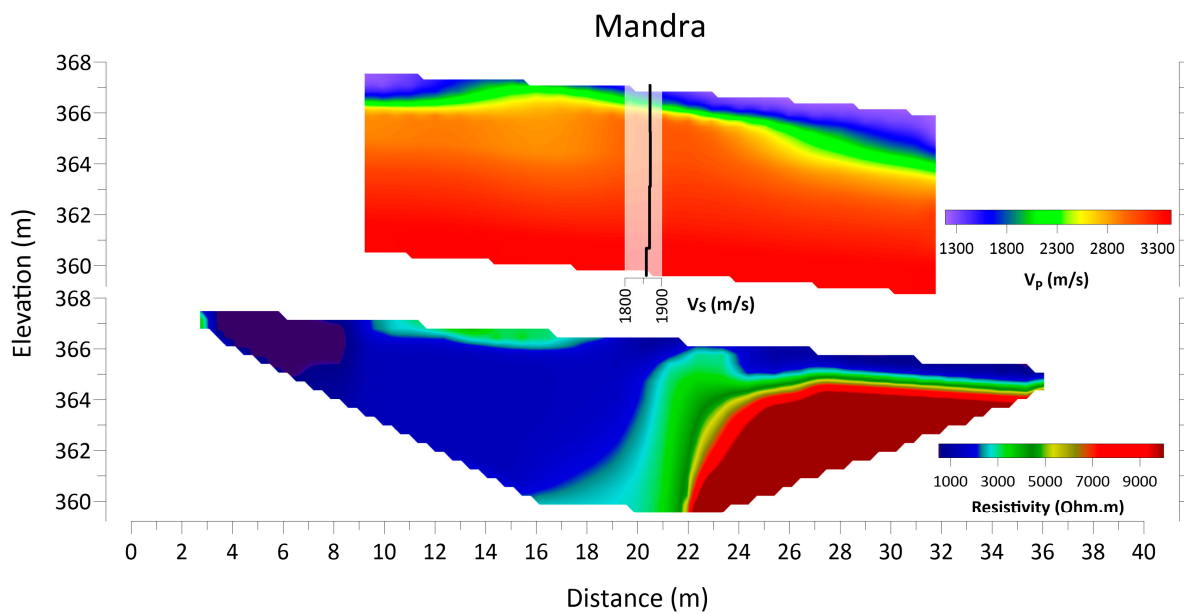


**Figure 5.** SRT and MASW (top) and ERT (bottom) sections at the site of the seismological station MDRA.

### 3.2. Seismological Station at Villia, Attica (VILL)

Station VILL (Figure 6) is situated at the children’s camps of Aspropyrgos municipality, near Villia town in western Attica, established on 12 October 2009. The station is currently equipped with a *Nanometrics Centaur CTR3-3S* datalogger and a *Trillium Horizon/120s* broadband seismometer, deployed in collaboration with the Ruhr-University Bochum as part of the AdriaArray project ([https://orfeus.readthedocs.io/en/latest/adria\\_array\\_main.html#](https://orfeus.readthedocs.io/en/latest/adria_array_main.html#), accessed on 25 March 2023). The station’s proximity to the eastern Gulf of Corinth [69,70], where a sequence of three major ( $M \geq 6.0$ ) earthquakes occurred in 1981, makes this site crucial for the monitoring of seismicity. The carbonate bedrock, where the station is based (Figure 6), comprises dolostones, dolomitic limestones, and limestones of the Upper Triassic (TRm) of the Sub-Pelagonian Unit [68], i.e., the same formation as the MDRA seismological station.



**Figure 6.** Location of the seismological station VILL and the geophysical measurements along with the geology of the area.

The HVSR curves for station *VILL* (Figure 7) present two types of behavior, due to a replacement in the instrumentation that took place on 7 October 2022. The previous seismometer was a *CMG-40T/30s* sensor; the new instrument is a *Trillium Horizon/120s*, considered of higher quality and more reliable. For the recordings before 7 October 2022 (old sensor), at higher frequencies ( $f > 5$  Hz) the HVSR seems to gradually drop, with the amplification factor reaching values below unity above 10.0 Hz. This does not occur with the new sensor, which presents a base level of amplification almost at 1.5 up to 12.0 Hz. In the latter case, a high-frequency peak can be distinguished in the HVSR, at  $f = 10.4$  Hz, with  $A = 1.9 \pm 0.3$ . We investigated whether this high peak could be an artifact of the specific instrument type, which is also installed on other sites, but there was no evidence that it is a systematic issue. Therefore, it is considered likely that the peak at  $f = 10.4$  Hz is real and simply could not be identified with the old sensor, which had problems at frequencies above 5.0 Hz.

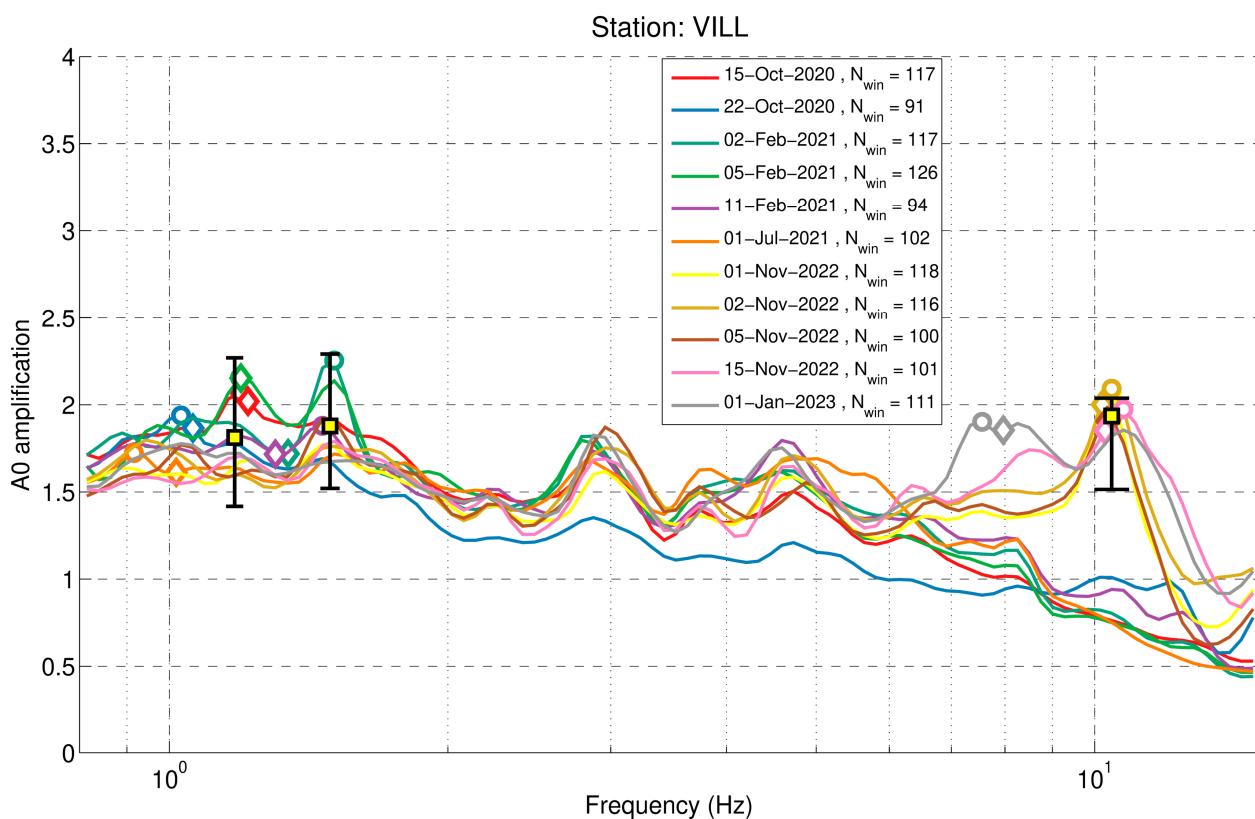


**Figure 7.** Average HVSR curves (solid lines) determined for station *VILL* on different days, from 60 s long windows selected after the application of STA/LTA anti-triggering on 6 h long records. Circles denote the global frequency on each curve, while diamond symbols mark the average of the frequency band denoting the range of peak frequencies of the HVSR lines from the individually selected windows (light/dark gray band in Figure 2b). Squares mark the prominent global and secondary peak frequencies recognized from the HVSR spectra, with error bars indicating the uncertainty of the amplification factor (Table A1).

In Figure 8, the results of the geophysical measurements at the site of the *VILL* seismological station are presented. Concerning the SRT technique, the seismic data processing revealed three seismic layers with velocities  $V_{P1} = 900$  m/s,  $V_{P2} = 1300$  m/s, and  $V_{P3} > 1700$  m/s, with average thickness of 1.0 m and 0.5 m for the first and the second layer, respectively. As mentioned above, the solid bedrock of the seismological station is the Triassic dolostones, which have also been found at the *MDRA* station. The relatively smaller depth of penetration and the lower value of P-wave velocity in this location is assumed to be caused by the possible karstification of the carbonate rocks present in the area. The

1D S-wave velocity model, derived from the MASW technique, revealed one seismic layer with velocity  $V_{S1} = 1160$  m/s, which is considered to be the velocity of the seismic bedrock, while the S-wave velocity for the first 30.0 m of the subsurface was calculated at 1217 m/s. Finally, the results of the ERT technique, also presented in Figure 6, revealed a resistant layer (>7000 Ohm.m), dominating across the section at depths greater than 0.5 m.

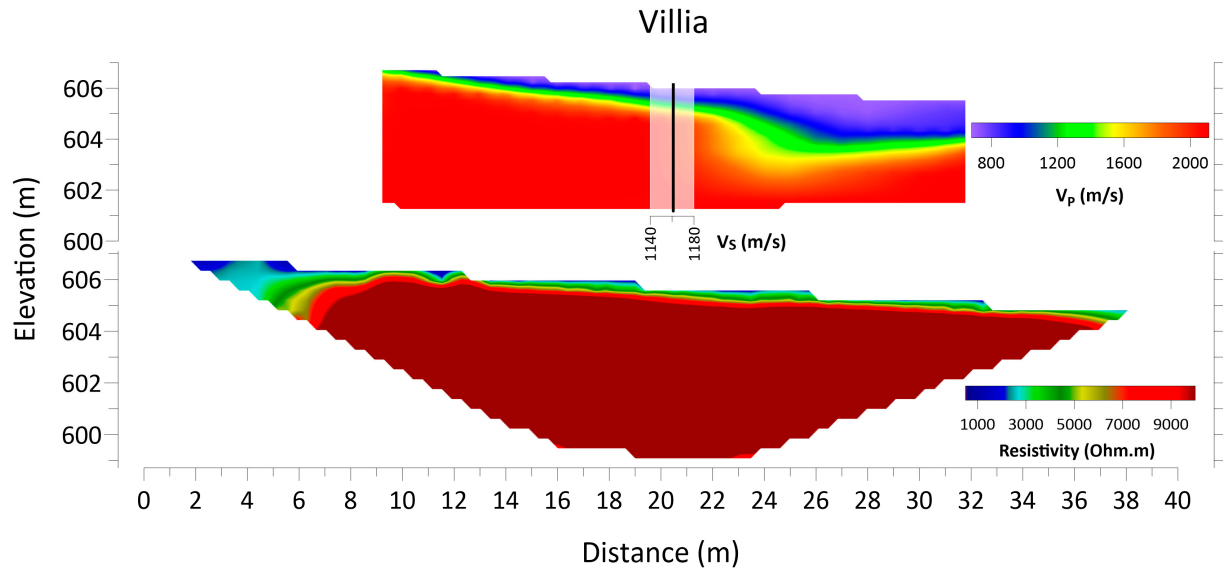


**Figure 8.** SRT and MASW (top) and ERT (bottom) sections at the site of the seismological station VILL.

### 3.3. Seismological Station at Loutraki, Korinthia (LOUT)

Station LOUT was installed on 27 May 2010 at the monastery of Prophet Ilias (Figure 9), near Loutraki town, south of Gerania Mt. Station LOUT is currently using a *Guralp CMG-DM24S6-EAM* datalogger, employing a *CMG-40T/30s* seismometer. The station is based on old cemented talus cones and scree (*Q.cn*) (Figure 7), which overlie in places the Middle Jurassic shales–chert formation (*sh*) and limestones (*Jm.k*) [71].



**Figure 9.** Location of the seismological station LOUT and the geophysical measurements along with the geology of the area.

The HVSR results at station *LOUT* (Figure 10) indicate some peak frequencies, but two of them seem the most important. A first frequency peak appears to be at  $f = 1.4 \pm 0.1$  Hz, with  $A = 2.3 \pm 0.5$ , and a secondary frequency peak at  $f = 5.1$  Hz, with  $A = 2.2 \pm 0.4$ . The base level of the amplification factor is equal to 1.8. Station *LOUT* has the same sensor as the old one of station *VILL* (*CMG-40T/30s*), which may be the cause of the observed gradual decrease of HVSR for frequencies  $>5.0$  Hz, likely masking any possible higher peak frequencies.

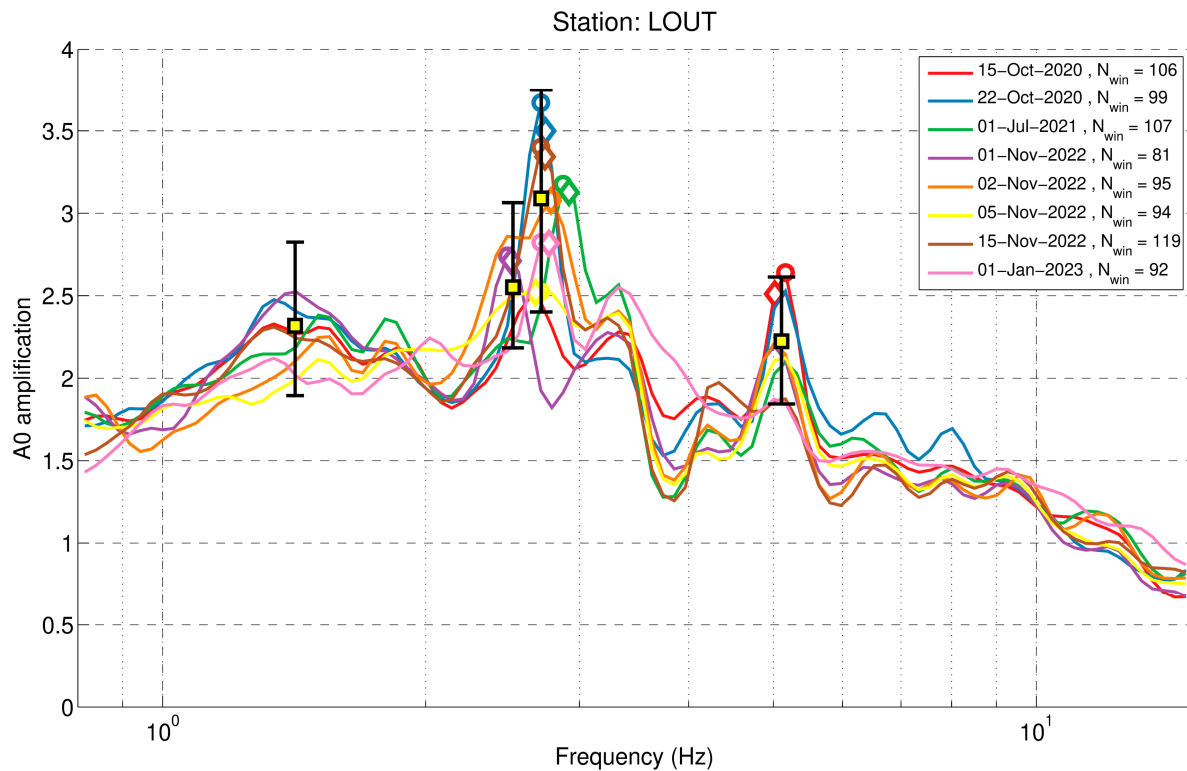


**Figure 10.** Average HVSR curves (solid lines) determined for station *LOUT* on different days, from 60 s long windows selected after the application of STA/LTA anti-triggering on 6 h long records. Circles denote the global frequency on each curve, while diamond symbols mark the average of the frequency band denoting the range of peak frequencies of the HVSR lines from the individually selected windows (light/dark gray band in Figure 2b). Squares mark the prominent global and secondary peak frequencies recognized from the HVSR spectra, with error bars indicating the uncertainty of the amplification factor (Table A1).

At *LOUT* seismological station, the results of the SRT technique (Figure 11) revealed three seismic layers with the following characteristics:  $V_{P1} = 700$  m/s,  $V_{P2} = 900$  m/s,  $V_{P3} > 1100$  m/s, and an average thickness of 2.5 m and 1.0 m for the first and second layer, correspondingly. According to the MASW technique (Figure 11), the shear-wave velocity of the seismic bedrock, below the first 5.0 m, was determined to be greater than 500 m/s. Finally, the  $V_{S30}$  value of the subsurface for the *LOUT* seismological station was calculated as 638 m/s. In Figure 11, the results derived from the processing of the ERT data are also presented. In the first 3.0 m, on average, a relatively resistant ( $>200$  Ohm.m) formation is present across the section. The resistivity value decreases ( $<100$  Ohm.m) with depth, as a result of the possible increase in the ambient moisture.

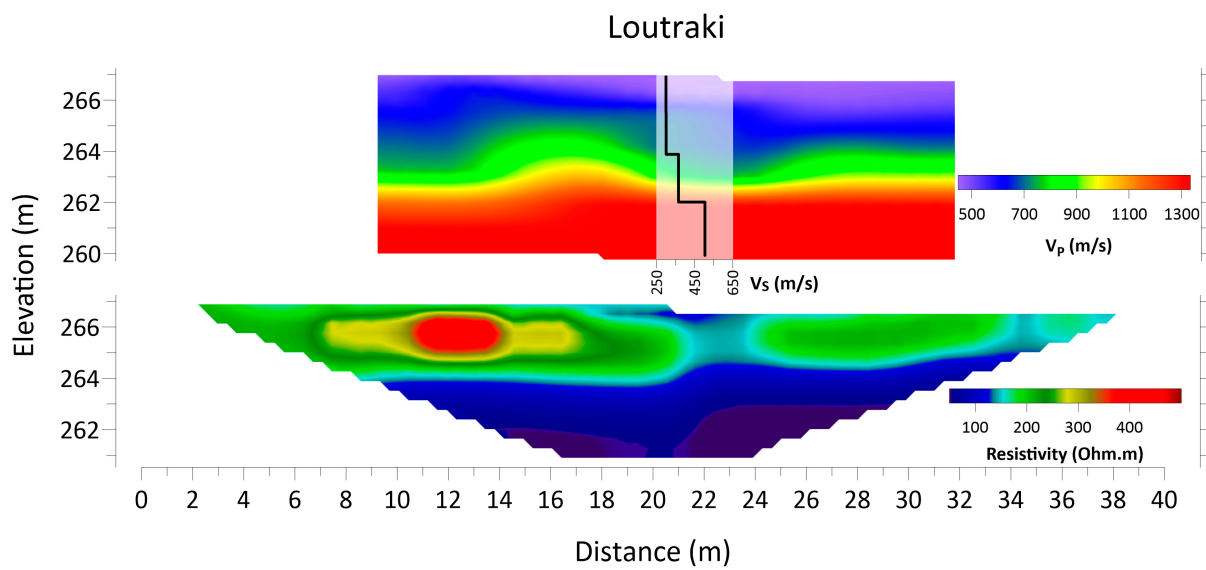


**Figure 11.** SRT and MASW (top) and ERT (bottom) sections at the site of the seismological station *LOUT*.

3.4. Seismological Station at Thalerio, Korinthia (*THAL*)

Station *THAL* (Figure 12) is located in the village of Thalerio, near the southern coast of the eastern Gulf of Corinth. The station was installed on 12 June 2008 and currently employs a *Guralp CMG-DM24S6-EAM* datalogger with a *CMG-40T/30s* seismometer.

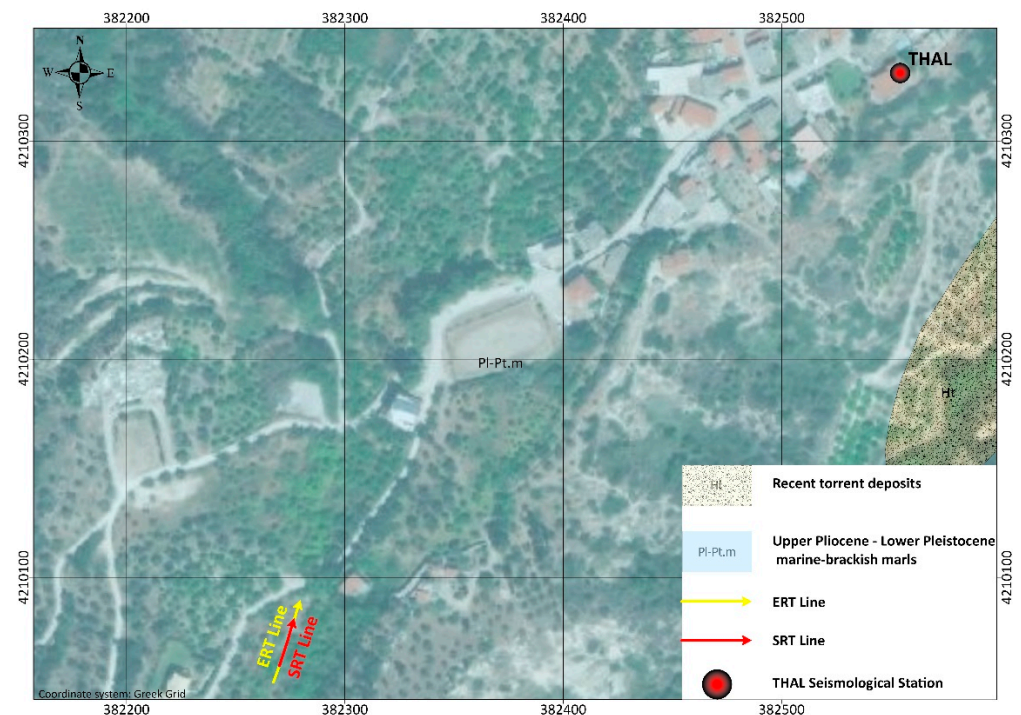


**Figure 12.** Location of the seismological station *THAL* and the geophysical measurements along with the geology of the area.

The area where the station is located (Figure 12) comprises Upper Pliocene to Lower Pleistocene marine-brackish marls, part of the *Megalos Valtos* formations (*Pl-Pt.m*). In places, recent torrent deposits (*Ht*) can be observed [72].

Station *THAL* has a fairly flat HVSR curve (Figure 13), with multiple local maxima but without any prominent global one. In most cases, a dominant peak frequency is found at  $f = 1.4\text{--}1.5$  Hz, with  $A = 1.7 \pm 0.4$ . A secondary peak can be observed in some cases at  $f = 2.3$  Hz, with  $A = 1.6 \pm 0.3$ . Although the instrument is the same as that at station *LOUT*, there is no observed gradual drop of the amplification factor at  $f > 5.0$  Hz, but a fairly constant base level at the amplification close to 1.5.

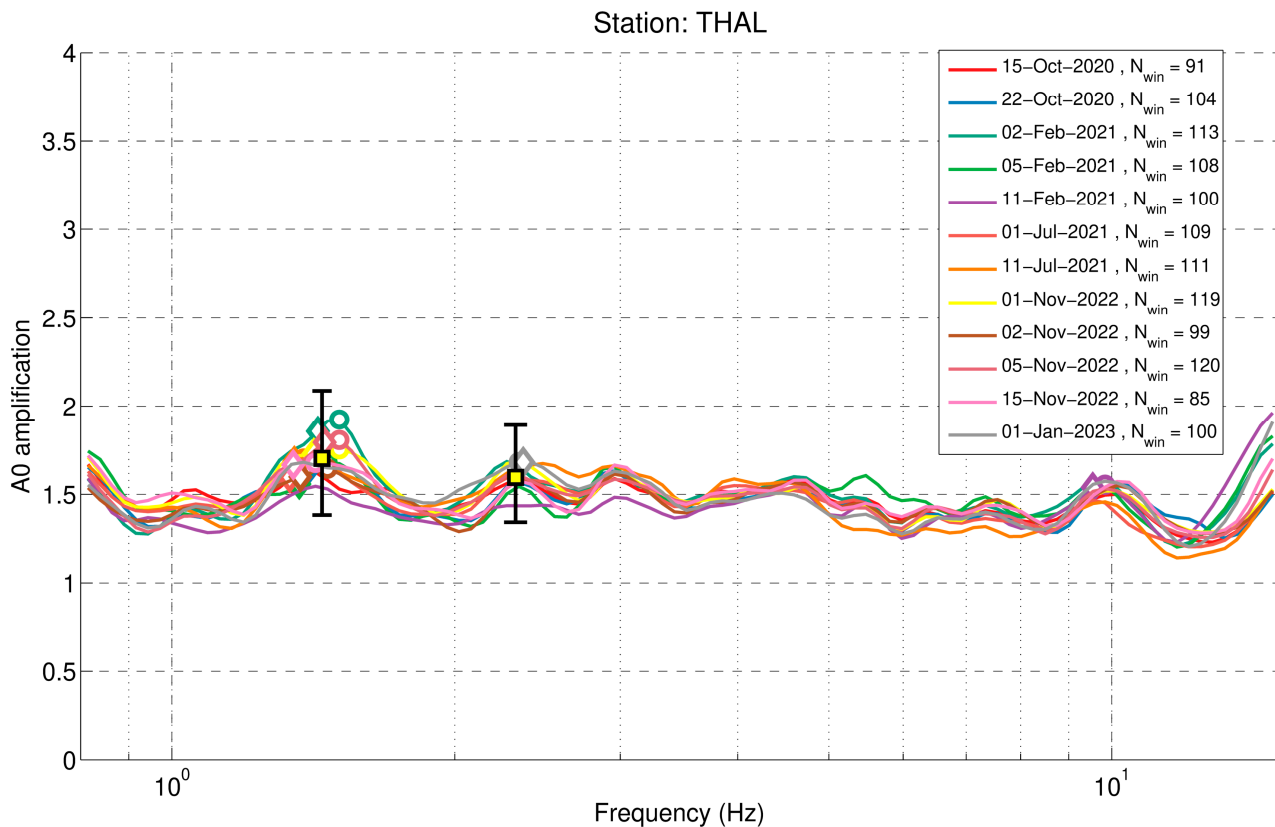


**Figure 13.** Average HVSR curves (solid lines) determined for station *THAL* on different days, from 60 s long windows selected after the application of STA/LTA anti-triggering on 6 h long records. Circles denote the global frequency on each curve, while diamond symbols mark the average of the frequency band denoting the range of peak frequencies of the HVSR lines from the individually selected windows (light/dark gray band in Figure 2b). Squares mark the prominent global and secondary peak frequencies recognized from the HVSR spectra, with error bars indicating the uncertainty of the amplification factor (Table A1).

The 2D seismic model (Figure 14) derived from the SRT technique revealed the existence of three seismic layers. The first layer has an average thickness of 3.0 m with a P-wave velocity value of  $V_{P1} = 550$  m/s. The second layer's average thickness is estimated at 0.5 m with  $V_{P2} = 900$  m/s. Finally, the third layer, which is considered the seismic bedrock, is present below the depth of 3.5 m and has a velocity value greater than 1300 m/s. Regarding the 1D, S-wave velocity distribution (Figure 14), the bedrock's shear-wave velocity was calculated as equal to 250 m/s. Furthermore, the S-wave velocity of the first 30.0 m was estimated at 300 m/s. According to the 2D distribution of the subsurface resistivity (Figure 14), two main geoelectrical layers were investigated. The first layer had an average thickness of 2.0 m and a resistivity value greater than 50.0 Ohm.m, whereas the second had a resistivity value below 50.0 Ohm.m, possibly affected by the subsurface moisture. At this point, we should mention that the geophysical line could not be executed closer to the station due to the inhabited character of the area and the stiff topography.

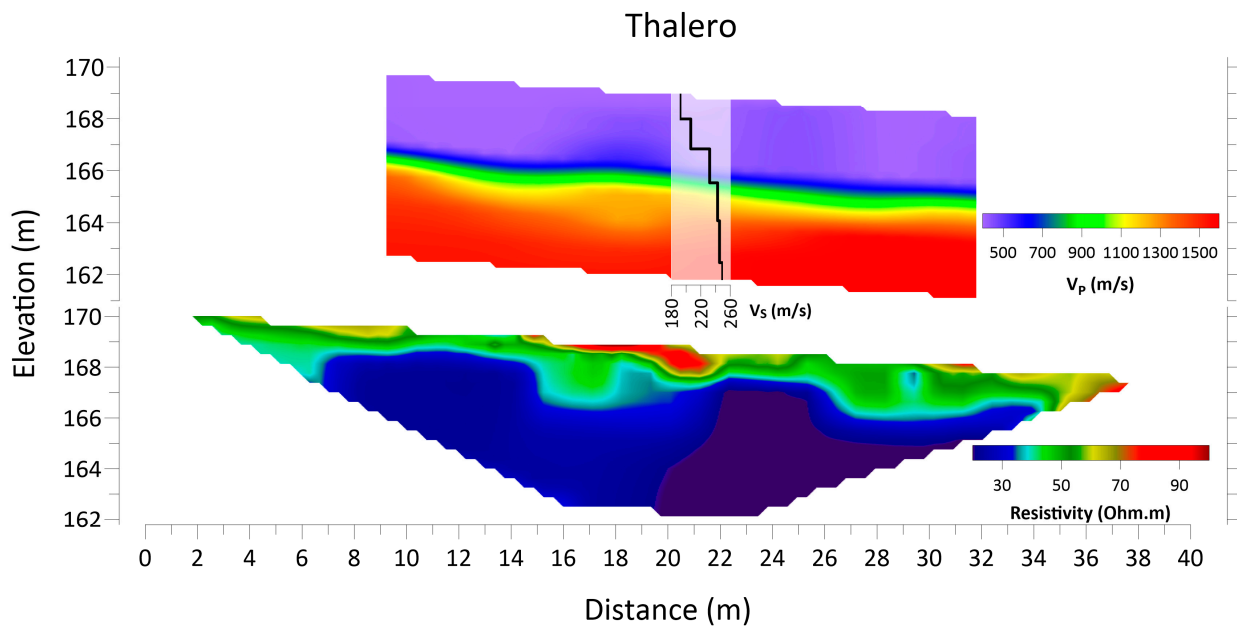


**Figure 14.** SRT and MASW (top) and ERT (bottom) sections at the site of the seismological station *THAL*.

### 3.5. Seismological Station at Atalanti, Fthiotida (*ATAL*)

Station *ATAL*, situated about 5 km north of Atalanti town (Figure 15), in Fthiotida, Central Greece, was installed on 26 September 2007. The site of this station is important for the monitoring of seismicity in the northern Euboikos Gulf. Station *ATAL* is presently equipped with a *Guralp CMG-DM24S6-EAM* datalogger and a *CMG-3T/120s* broadband seismometer. The geophysical line could not be executed closer to the station due to the rough geomorphology of the area in its vicinity and the vegetation.



**Figure 15.** Location of the seismological station *ATAL* and the geophysical measurements along with the geology of the area.

The carbonate bedrock, where the station is based (Figure 15), consists of Middle and Lower Jurassic limestones and dolomites (*Ji-m kD*), according to [73].

Similar to the case of station *THAL*, station *ATAL* also presents a fairly flat HVSR curve (Figure 16). However, the base level of amplification is lower, with an average value equal to 1.1. A frequency peak at  $f = 1.0$  Hz, with  $A = 1.3 \pm 0.3$ , is present in some cases, but it is not clear. A higher peak frequency at  $f = 13.6$  Hz, with  $A = 1.2 \pm 0.2$ , is also distinguished in some of the cases.

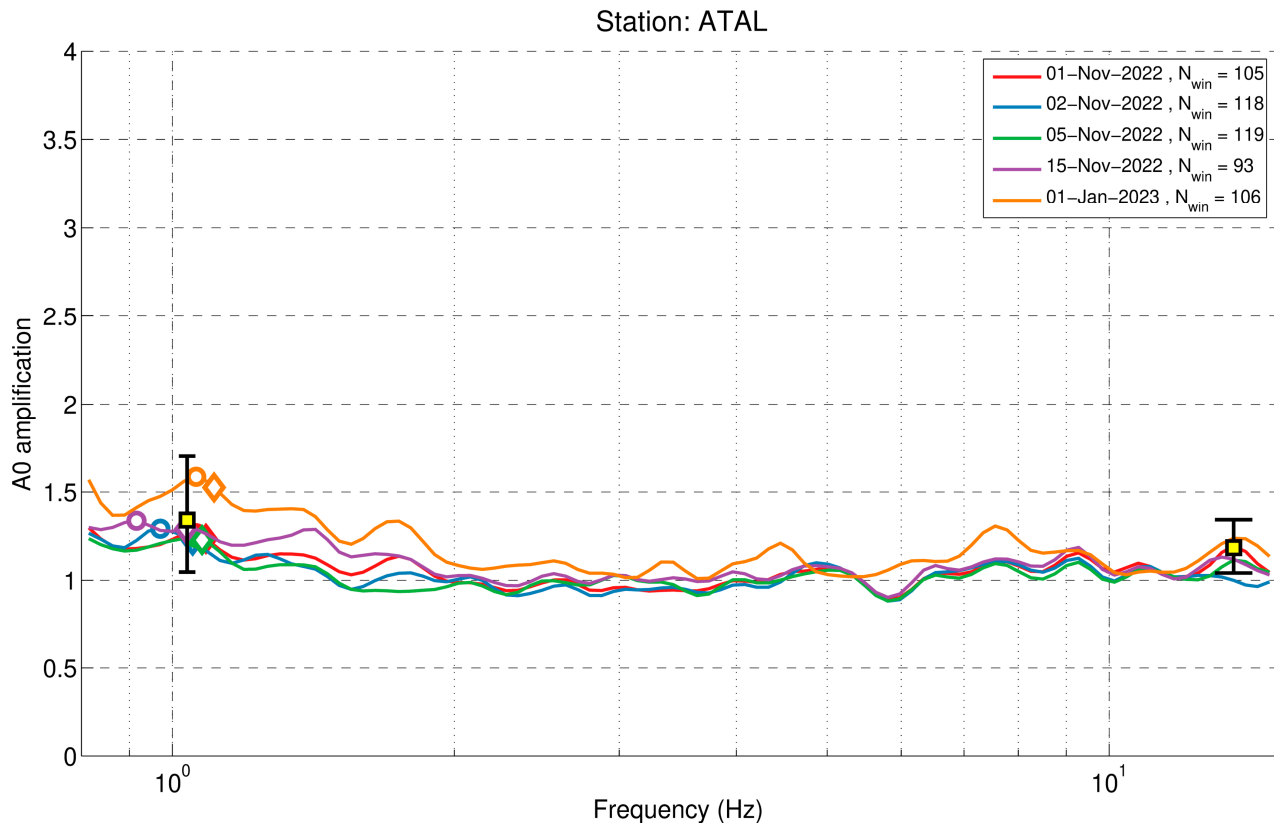


**Figure 16.** Average HVSR curves (solid lines) determined for station *ATAL* on different days, from 60 s long windows selected after the application of STA/LTA anti-triggering on 6 h long records. Circles denote the global frequency on each curve, while diamond symbols mark the average of the frequency band denoting the range of peak frequencies of the HVSR lines from the individually selected windows (light/dark gray band in Figure 2b). Squares mark the prominent global and secondary peak frequencies recognized from the HVSR spectra, with error bars indicating the uncertainty of the amplification factor (Table A1).

Concerning the SRT technique (Figure 17) at *ATAL* seismological station, the subsurface consists of three seismic layers. The first and second layers have an average thickness of 1.0 m each and P-wave velocities of  $V_{P1} = 1200$  m/s and  $V_{P2} = 1900$  m/s, respectively. At depths greater than 2.0 m, the seismic bedrock dominates along the section with  $V_{P3} > 2700$  m/s. Additionally, the S-wave velocity of the seismic bedrock was calculated at 1940 m/s, as derived from the 1D MASW model (Figure 17), while the  $V_{S30}$  value was determined at 2016 m/s. The results of the ERT (Figure 17) reveal a significantly resistant ( $>8000$  Ohm.m) formation across almost the entire section.

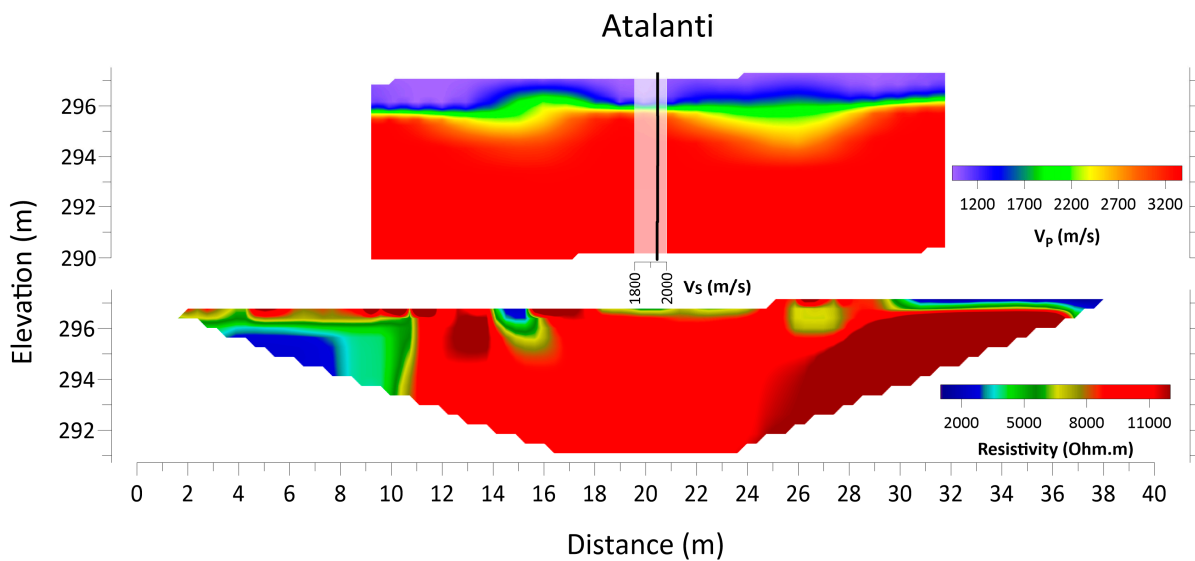


**Figure 17.** SRT and MASW (top) and ERT (bottom) sections at the site of the seismological station ATAL.

3.6. Seismological Station at Epidavros, Argolis (EPID)

Station EPID, located at Kalamiou monastery (Figure 18), near the town of Epidavros in eastern Peloponnese, was deployed on 8 October 2010. The site is important for the monitoring of the seismic activity in the southern Saronikos Gulf, which hosts the Methana volcano, at the north-western end of the Hellenic volcanic arc. Station EPID is currently equipped with a Guralp CMG-DM24S6-EAM datalogger and a CMG-40T/30s seismometer. The area consists of undivided Quaternary sediments and soils (Q), which overlie the Middle-Upper Triassic chert limestones (T2-4 k, hn) and the Lower Triassic trachytes and trachytic tuffs ( $\tau$ , tf), as described by [74].

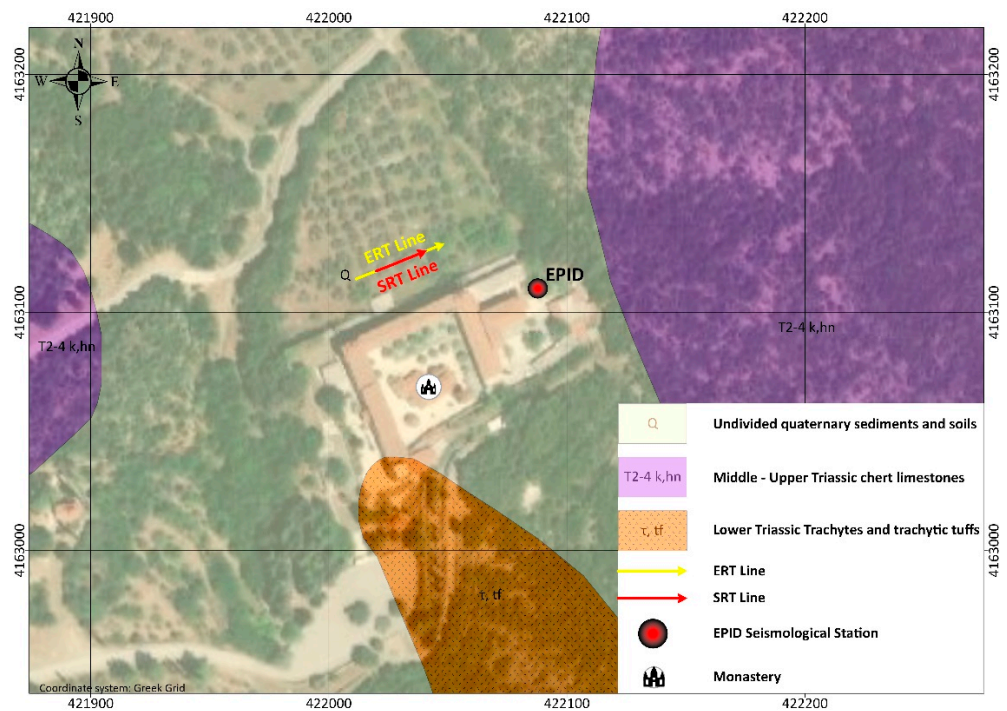


**Figure 18.** Location of the seismological station EPID and the geophysical measurements along with the geology of the area.

The HVSR curves for station *EPID* (Figure 19) show a clear but broad peak frequency at  $f = 6.5$  Hz, with  $A = 2.3 \pm 0.8$ . The base amplification level for station *EPID* is close to 0.8, which is lower than unity, indicating that the amplification factors could be underestimated by 0.2. Higher values of amplification are acquired when using a square average for the horizontal components. In that case, the base level is equal to 1.1, and the peak frequency at 6.5 Hz has an amplification factor equal to  $2.5 \pm 0.8$ .

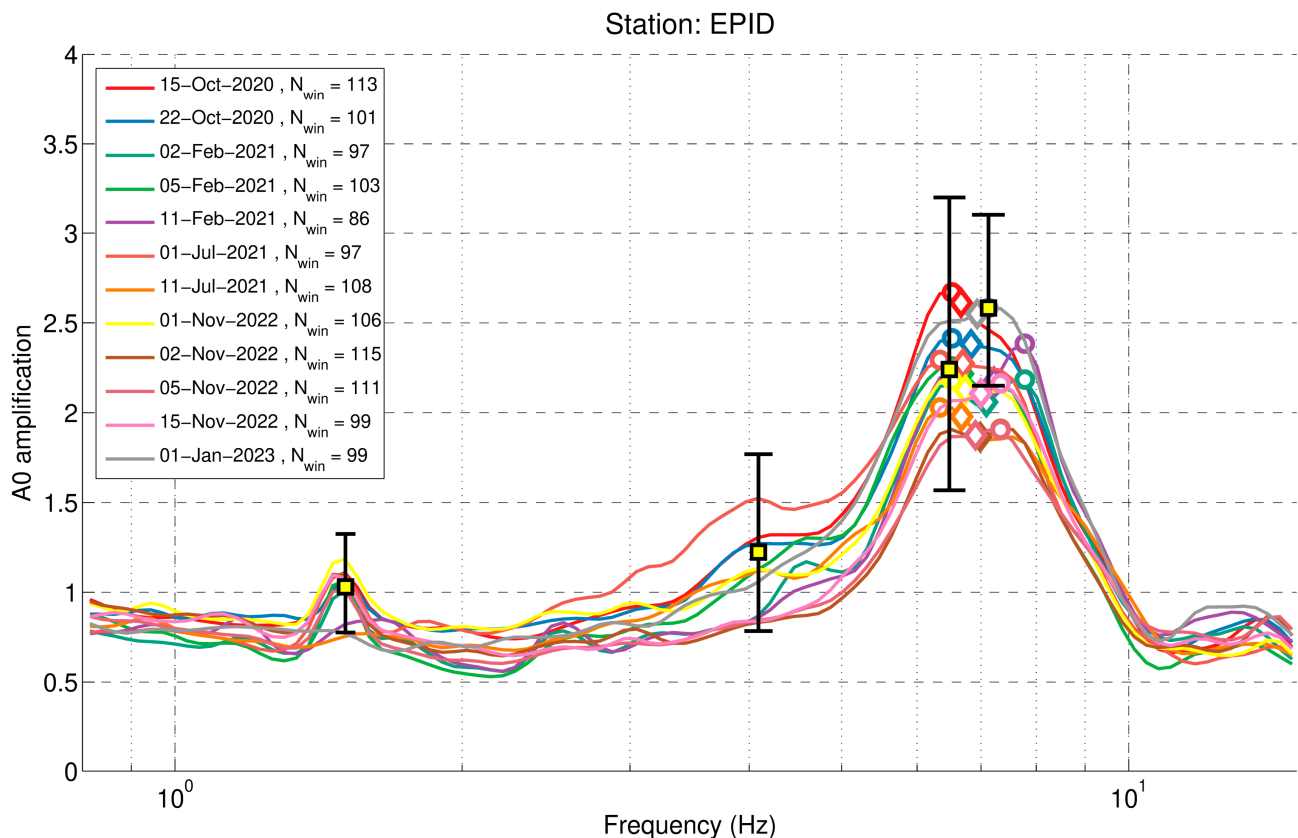


**Figure 19.** Average HVSR curves (solid lines) determined for station *EPID* on different days, from 60 s long windows selected after the application of STA/LTA anti-triggering on 6 h long records. Circles denote the global frequency on each curve, while diamond symbols mark the average of the frequency band denoting the range of peak frequencies of the HVSR lines from the individually selected windows (light/dark gray band in Figure 2b). Squares mark the prominent global and secondary peak frequencies recognized from the HVSR spectra, with error bars indicating the uncertainty of the amplification factor (Table A1).

At the seismological station of Epidavros (*EPID*), three seismic layers were identified through the SRT technique (Figure 20). The first and second layers develop after the first 5.0 m of the SRT section, with an average thickness of 2.0 m and 1.0 m, respectively. Their P-wave velocity values were determined to be equal to  $V_{P1} = 600$  m/s and  $V_{P2} = 750$  m/s. Finally, below these layers, the existence of the seismic bedrock was defined with  $V_{P3} > 800$  m/s. The MASW technique (Figure 20) revealed a seismic bedrock shear-wave velocity of 350 m/s and a  $V_{S30}$  value equal to 393 m/s. In Figure 20, the 2D distribution of the subsurface resistivity is also presented. At the central parts of the section and at depths above 4.0 m, a relatively resistant ( $>600$  Ohm.m) formation is investigated. Below that, a more conductive formation dominates across the section with a resistivity value lower than 300 Ohm.m.

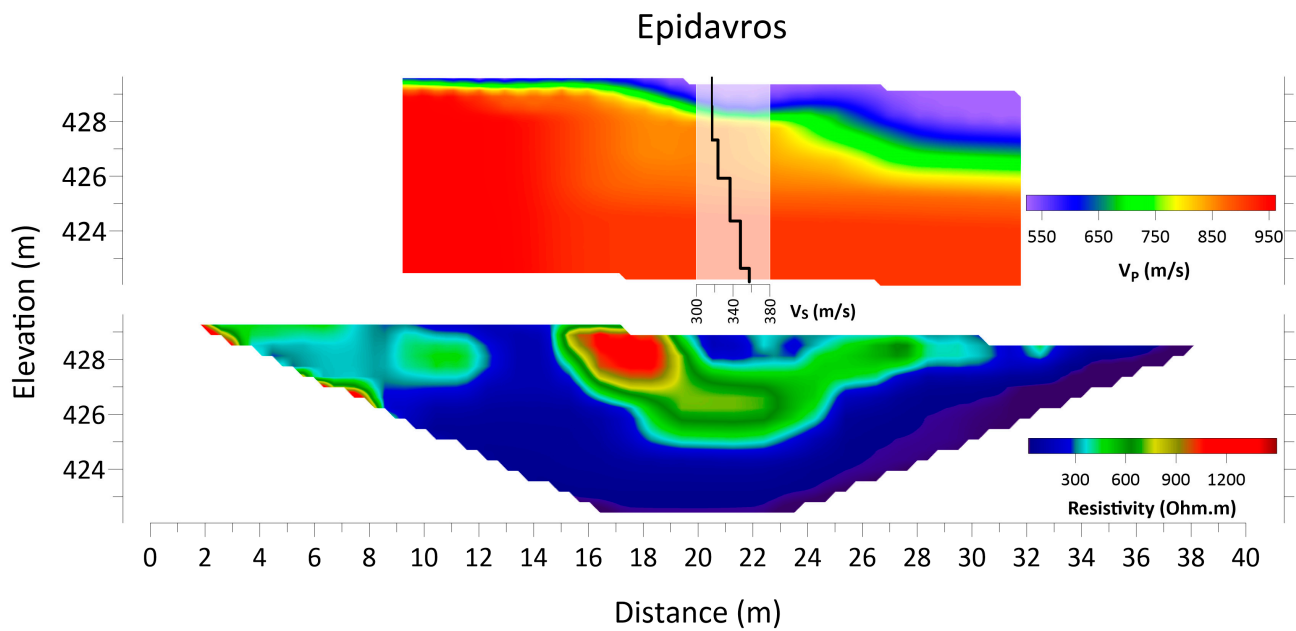


**Figure 20.** SRT and MASW (top) and ERT (bottom) sections at site of the seismological station EPID.

#### 4. Determination of Elastic Moduli

In the context of site characterization of the selected seismological stations of the Athenet seismological network, the elastic moduli presented in Table 3 were calculated, i.e., the Poisson's ratio ( $\sigma$ ), the shear modulus ( $G$ ), the Young's modulus ( $E$ ), and the bulk modulus ( $K$ ). The Poisson's ratio ( $\sigma$ ) specifies the ratio of the deformation perpendicular to the deformation parallel to the applied stress. It is a non-dimensional elastic modulus, with values ranging between 0.1 and 0.5, corresponding to the compact and loose formations, respectively. The Young's modulus ( $E$ ) is the ratio between the longitudinal stress to the longitudinal strain, referring to an elastic solid exposed under uniaxial compression or extension. For the calculation of the shear modulus ( $G$ ), the  $V_s$  and density values are required as an input to the relationship  $G = \rho V_s^2$  ( $V_s$  in m/s and  $\rho$  in  $\text{g}/\text{cm}^3$ ). Finally, the bulk modulus ( $K$ ) describes the deformation of the volume of a medium which is under pressure. The calculation approach of the elastic moduli with the contribution of geophysical and density measurements has been successfully applied in previous studies [58,75–79].

**Table 3.** Elastic moduli equations.

Elastic Modulus	Equation	Reference
Poisson's ratio ( $\sigma$ )	$\sigma = \frac{1}{2} \left[ 1 - \frac{1}{(V_p/V_s)^2 - 1} \right]$	[80]
Young's modulus ( $E$ )	$E = \rho \frac{3V_p^2 - 4V_s^2}{(V_p/V_s)^2 - 1}$	[80]
Shear modulus ( $G$ )	$G = \frac{E}{2(1+\sigma)}$	[81]
Bulk modulus ( $K$ )	$K = \frac{E}{3(1-2\sigma)}$	[81]

The density values used for the calculation of the above elastic moduli are presented in Table 4, while the P- and S-wave velocities were determined by the seismic profiles of the SRT and MASW techniques, at each seismological station. Additionally, in Table 4, the median values of all the above-mentioned parameters for every geological formation, at each location, are presented.

**Table 4.** Seismic velocities and calculated elastic moduli of the geological formations.

Station Name	Geological Formations	$V_P$ (m/s)	$V_S$ (m/s)	Density (gr/cm <sup>3</sup> )	$\sigma$	$G$ (GPa)	$E$ (GPa)	$K$ (GPa)	$\rho$ (Ohm.m)
MDRA	Dolostones (TRm)	3300	1860	2.69	0.27	9.31	23.59	22.31	9000
VILL	Dolostones (TRm)	2100	1160	2.66	0.28	3.58	9.17	9.05	8000
LOUT	Talus cones (Q.cn)	1330	500	2.30 [62,63]	0.42	0.58	1.63	3.64	100
THAL	Marls (Pl-Pt.m)	1600	250	1.72 [62,63]	0.49	0.11	0.32	4.32	50
ATAL	Limestones (Ji-m kD)	3300	1940	2.81	0.24	10.58	26.14	22.67	9000
EPID	Trachytes and trachytic tuffs ( $\tau$ , $tf$ )	950	350	2.04 [67]	0.42	0.25	0.71	1.65	250

## 5. Results and Discussion

In this study, the results of the applied geophysical methods that have been employed to determine the essential key parameters for the site characterization of the selected seismological stations have been presented. Certain parameters are directly determined by the processing results (e.g.,  $V_S$  and  $V_{S30}$ ) or can simply be calculated; the seismic bedrock  $h_{seis}$  is derived from the equation  $h_{seis} = V_S/4 f_0$ , where  $V_S$  is the average shear-wave velocity in the sediment layer and  $f_0$  is the fundamental frequency [82]. Other parameters are provided based on the classification of the calculated parameters (e.g., soil type based on  $V_{S30}$ ) or may need further interpretation (e.g., subsurface geology). Therefore, for the required parameter of the subsurface geology at each seismic station, the results of the SRT and ERT techniques (Figures 5, 8, 11, 14, 17 and 20) have been interpreted and are discussed below for each station. Taking into account the calculated  $V_{S30}$  values, the corresponding ground-type classification of each site has been determined (Table 5), based on Eurocode 8 [58].

**Table 5.** Key parameters for site characterization of seismic stations.

Station Name	Fundamental Frequency, $f_0$ (Hz)	Seismic Bedrock Depth, $H_{seis}$ (m)	$V_S$ (m/s)	$V_{S30}$ (m/s)	Soil Type (EC8) [58]	Subsurface Geology
MDRA	-	-	1830–2500	1877	A	Dolostones, dolomitic limestones, and limestones
VILL	10.4	13.0	1160–1500	1217	A	Dolostones, dolomitic limestones, and limestones
LOUT	2.7	30.0	300–900	638	B	Old talus cones and scree formation, shales–chert, and limestone formations
THAL	1.4	54.0	200–420	300	C	Marine-brackish marls and conglomerates
ATAL	-	-	1930–2350	2016	A	Limestones and dolomites
EPID	7.1	12.0	320–460	393	B	Quaternary sediments, trachytes/trachytic tuffs, and chert limestones

The geophysical measurements at the seismological stations *MDRA* (Figure 5) and *VILL* (Figure 8) have been carried out on the same geological formation, which is dolostones, dolomitic limestones, and limestones of the Upper Triassic (*TRm*). The revealed subsurface geophysical structure, corresponding to resistivity values greater than 7000 Ohm.m and  $V_p$  greater than 1700 m/s, could be interpreted as the extension in depth of the same carbonate formation. At the *MDRA* station, a geoelectrical formation of 1000 Ohm.m has also been revealed, probably due to the water saturation of the formation. Likewise, the ERT and SRT results at the *ATAL* station (Figure 17) seem to reveal the subsurface existence of the compact bedrock of Jurassic limestones and dolomites (*Ji-m kD*). The corresponding resistivity and  $V_p$  values are 8000 Ohm.m and 2700 m/s, which are similar to those of the *MDRA* station. The relatively lower value of P-wave velocity at the *VILL* station is assumed to be caused by the possible karstification of the carbonate rocks present in the area.

The fact that the solid, hard carbonate formations (*TRm* and *Ji-m kD*) are almost up to the surface at the station sites of *MDRA*, *VILL*, and *ATAL*, affected both the MASW and the HVSR techniques. The inability to record the high-frequency content of the surface waves is the reason the 1D velocity models, derived by the MASW technique, are reliable from a certain depth, which seems to be 12 m for the *MDRA* and *ATAL* stations (Figures A2 and A5) and 8 m for the *VILL* station (Figure A3). Thus, the  $V_s$  average values of the low-thickness sediments at these sites were estimated by converting the  $V_p$  values (SRT technique), based on the relationship  $V_p = 1.7 \cdot V_s$ .

The H/V curves at the prementioned sites were complicated, with multiple low amplitudes and no clear peaks. More specifically, the H/V curves at the *MDRA* station (Figure 4) show two close frequency peaks at 2.3 and 2.7 Hz, which could be an indication of the lateral irregularities inside the carbonate bedrock, possibly caused by the existence of the karst bauxite formation. At frequencies greater than 5.5 Hz, the H/V curves seem to be around an amplitude equal to 1.0, indicating the presence of the carbonate seismic bedrock. Therefore, no peak could be selected as the fundamental frequency peak at the *MDRA* station. According to the H/V curves at the *ATAL* station (Figure 16), no frequency peak could also be selected as the fundamental one, while the total form of the curves is the result of the presence of the carbonate hard rock formation almost at the surface. Regarding the H/V curves at the *VILL* station (Figure 7), a high-frequency peak at 10.4 Hz was identified after the replacement of the recording instrument, which was interpreted as the fundamental frequency peak of the site (Table 5). With an average  $V_s$  value of 530 m/s of the overlying sediments, converted from the  $V_p$  value of 900 m/s, the depth of the seismic bedrock was calculated equal to 13.0 m. This outcome is consistent with the results of the SRT and ERT techniques but also with the local geology. The relatively low  $V_p$  values (1700–2000 m/s) and high resistivity values (>7000 Ohm.m) can be related to the karstification of the carbonate formation, which justifies that the compact seismic bedrock may be present at depths greater than 13.0 m.

Given the fact that the geophysical results at the *LOUT* seismological station reveal relatively low values of elastic-wave velocities and resistivity (Figure 11), it is assumed that the maximum depth of investigation was not enough to overcome the thickness of the old talus cones and scree formation and, consequently, did not reach the inferred bedrock of the Middle Jurassic limestone formation (*Jm.k*). Regarding the MASW technique, a broadband frequency spectrum was recorded, extending the investigation depth down to 40 m (Figure A4). The H/V curves for this site (Figure 10) show two clear peaks at 2.7 and 5.1 Hz, with the lower frequency peak being interpreted as the fundamental one. With an average calculated shear-wave velocity equal to 320 m/s for the overlying sediments, the corresponding depths of the 2.7 and 5.1 Hz peaks were estimated equal to 30.0 and 16.0 m, respectively. Taking into consideration the local geology, the higher frequency peak at 5.1 Hz is probably attributed to the contrast impedance between the talus cones–scree and the shales–chert formations, while the lower frequency peak at 2.7 Hz is probably attributed to the shales–chert and the limestone formations. Additionally, the transition from the talus cones–scree to the shales–chert formation at the depth of 16.0 m is visible to the 1D  $V_s$

model, from the MASW technique (Figure A4), as below that depth the  $V_s$  value is around 900 m/s.

The geophysical subsurface investigation at station *THAL* revealed low resistivity values (close to 50 Ohm) and relatively low P-wave velocity values (550–1300 m/s) (Figure 14), which seem to correspond to the great thickness of the post-alpine marine-brackish marls (*Pl-Pt.m*); no hard rock basement is depicted. This is also consistent with the 1D  $V_s$  model derived from the MASW technique (Figure A5), where relatively low shear-wave velocities, with an average value of 300 m/s, are present until the depth of 28.0 m. Regarding the H/V curves (Figure 13), a fundamental frequency peak could be interpreted at 1.4 Hz. With an average  $V_s$  velocity of 300 m/s, the 1.4 Hz peak corresponds to a depth of 54.0 m (Table 5). This peak may be caused by the contrast impedance between the marine-brackish marls and underlain compact conglomerate formation that exist in the area. The multiple peaks that are present in the entire spectrum above 2.0 Hz indicate several lithological variations inside the marine-brackish marls formation, known also from the geological description of the formation.

The geophysical results at the seismological station *EPID* (Figure 20) reveal comparably low resistivity values and seismic velocities. These could be explained by the existence of Quaternary sediments (*Q*). Regarding the 1D  $V_s$  model from the MASW technique (Figure A7), the Quaternary deposits could extend down to a depth of 13 m with an average shear-wave velocity of 350 m/s. From the depth of 13.0 m until the depth of 30.0 m, the shear-wave velocity rises to an average value of 430 m/s, probably due to the existence of the trachytes and trachytic tuffs ( $\tau$ , *tf*) formation underlying the Quaternary sediments. Two clear peaks were identified in the H/V curves (Figure 19), at 1.5 and 7.1 Hz. With an average  $V_s$  value of 350 m/s, these peaks correspond to 58.0 and 12.0 m depths, respectively. The 7.1 Hz peak (12 m depth) could be related to the existence of a high impedance contrast between the quaternary sediments (*Q*) and the trachytes/trachytic tuffs ( $\tau$ , *tf*) formation and can be interpreted as the fundamental one (Table 5). Furthermore, this broad frequency peak indicates that subsurface structural variations (thickness and transition zones) also exist.

## 6. Conclusions

Four geophysical techniques have been implemented in the context of an applied multidisciplinary geophysical survey at selected seismological stations of the Athenet network. Accordingly, Seismic Refraction Tomography (SRT), Multichannel Analysis of Surface Waves (MASW), the Horizontal to Vertical Spectral Ratio (HVSR) technique, and Electrical Resistivity Tomography (ERT) have been carried out at the location of each seismological station in order to determine the essential information regarding the site characterization of their subsurface. The new information derived by this geophysical survey contributes to the amplification factors for each site that can lead to a more accurate calculation of Peak Ground Acceleration (PGA) or Peak Ground Velocity (PGV) and, therefore, to reliable Probabilistic and Stochastic Seismic Hazard Assessment. Additionally, for the determination of the Uniform Hazard Spectra (UHS), the derived Spectral acceleration ( $S_a$ ) values would have fewer uncertainties due to the implementation of the soil factors. The measurement of accurate  $V_{S30}$  values for each station of HUSN could help in the development of improved Ground Motion Prediction Equations (GMPEs) for the Greek region.

Based on the multidisciplinary geophysical data, important parameters have been determined, including the fundamental frequency ( $f_0$ ), shear-wave velocity distribution ( $V_s$ ), average shear-wave velocity in the upper 30 m of the site ( $V_{S30}$ ), depth of seismic ( $H_{seis}$ ) bedrock, surface geology, and soil-type classification at each site. Additionally, the calculation of selected elastic moduli (Poisson's ratio, shear, bulk, and Young's moduli) have also been carried out. However, at two stations (*MDRA* and *ATAL*), we were not able to determine the fundamental frequency and the depth of the seismic bedrock because of the deployment of the seismological station directly on hard rock, carbonate formations. This condition negatively affected both the MASW and the HVSR techniques at the seismological

stations of *MDRA*, *VILL*, and *ATAL*. Due to the inability to record the high-frequency content of surface waves, the MASW-technique-derived 1D velocity models are only reliable below a certain depth.

**Author Contributions:** Conceptualization, J.D.A., N.V. and G.K.; methodology, J.D.A., S.D., N.V. and G.K.; software, S.D., V.G., I.-K.G. and V.K.; validation, J.D.A., S.D., V.G., I.-K.G. and V.K.; investigation, J.D.A., S.D., V.G. and I.-K.G.; resources, J.D.A. and N.V.; data curation, J.D.A., S.D., V.G., I.-K.G. and V.K.; writing—original draft preparation, S.D., V.G., I.-K.G. and V.K.; writing—review and editing, J.D.A., S.D., G.K. and V.K.; visualization, S.D., V.G., I.-K.G. and V.K.; supervision, J.D.A., N.V. and S.D.; funding acquisition, J.D.A. and N.V. All authors have read and agreed to the published version of the manuscript.

**Funding:** The project was funded by “HELPOS-Hellenic System for Lithosphere Monitoring” (MIS 5002697), which is implemented under the action “Reinforcement of the Research and Innovation Infrastructure”, funded by the Operational Programme “Competitiveness, Entrepreneurship and Innovation” (NSRF 2014-2020) and co-financed by Greece and the European Union.

**Data Availability Statement:** Data available upon request.

**Acknowledgments:** The authors would like to thank Petras Athanasios and Aspasia Charalabopoulou for their valuable contribution during fieldwork measurements.

**Conflicts of Interest:** The authors declare no conflict of interest.

## Appendix A

### SRT and MASW seismic arrays layout

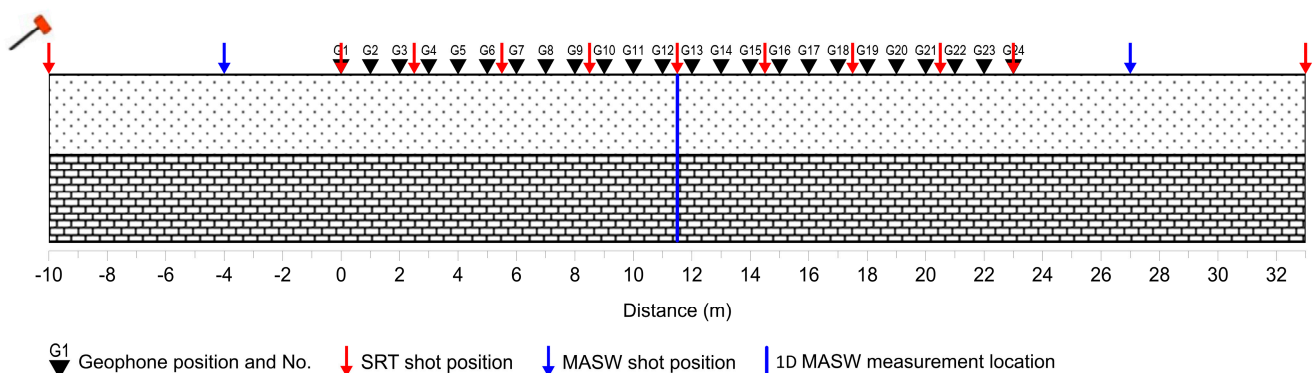


**Figure A1.** Sketch illustrating the locations of the shots and the arrangements of the geophones for the SRT and MASW seismic arrays.

## Appendix B

In Figures [A2–A7](#) the full 1D Vs models derived from the MASW technique at each seismological station are provided.

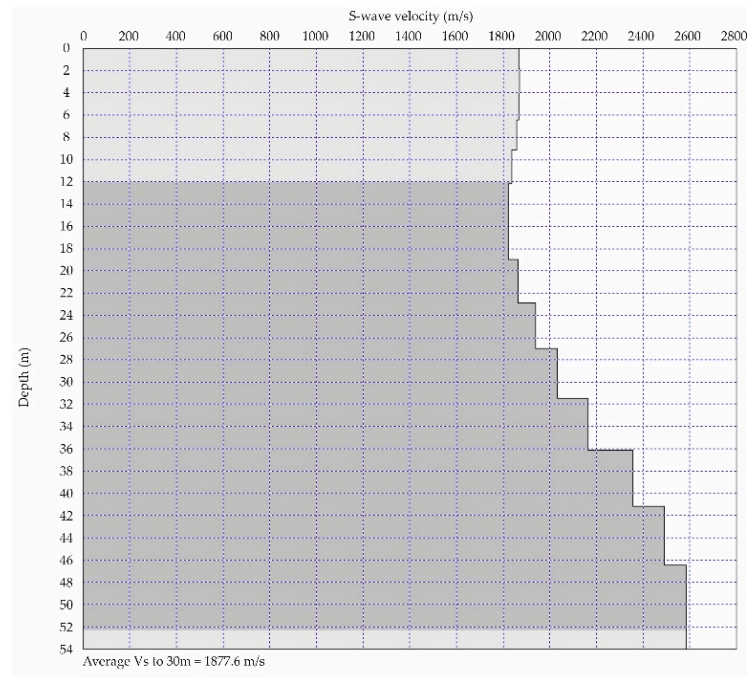


Figure A2. 1D Vs model derived from the MASW technique at MDRA station.

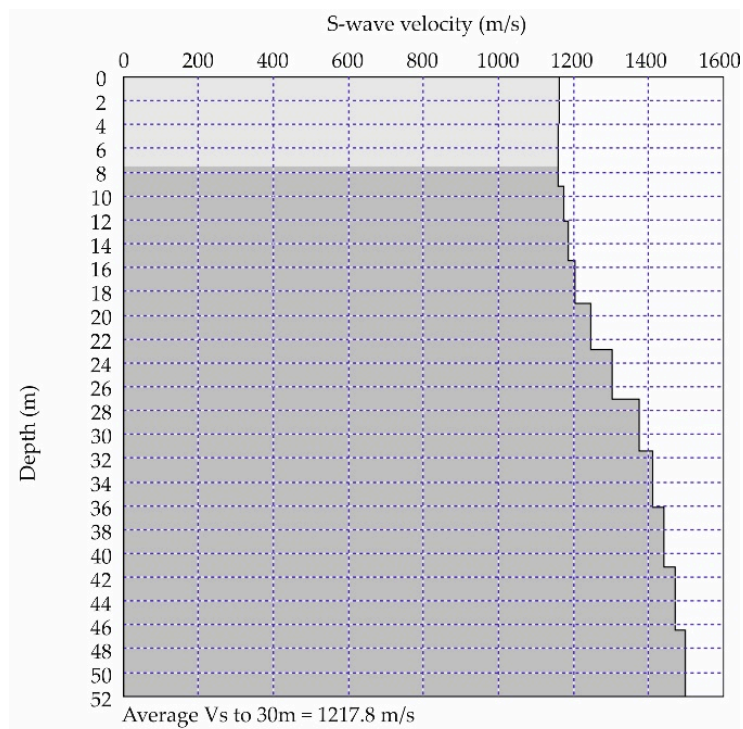


Figure A3. 1D Vs model derived from the MASW technique at VILL station.

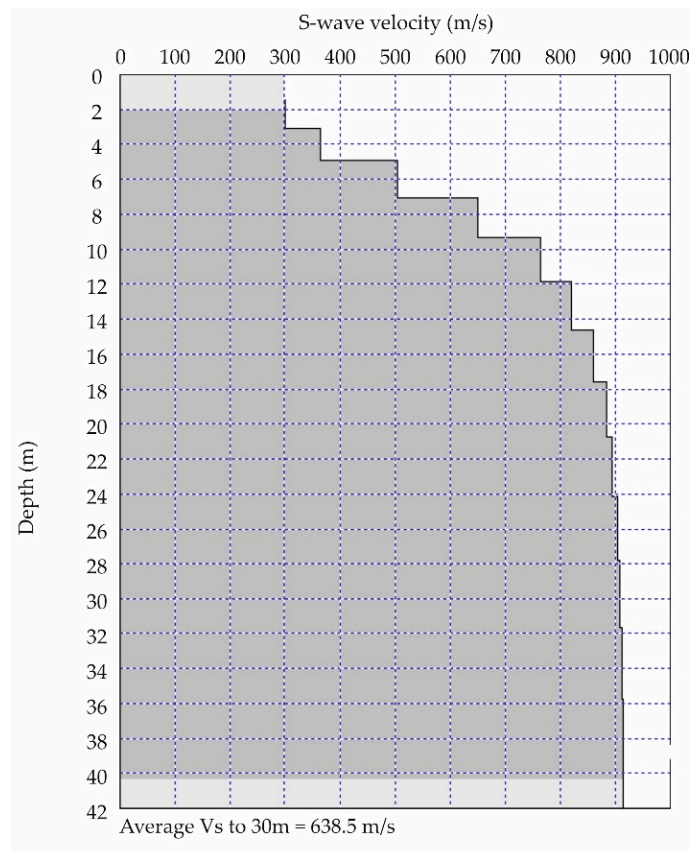


Figure A4. 1D Vs model derived from the MASW technique at LOUT station.

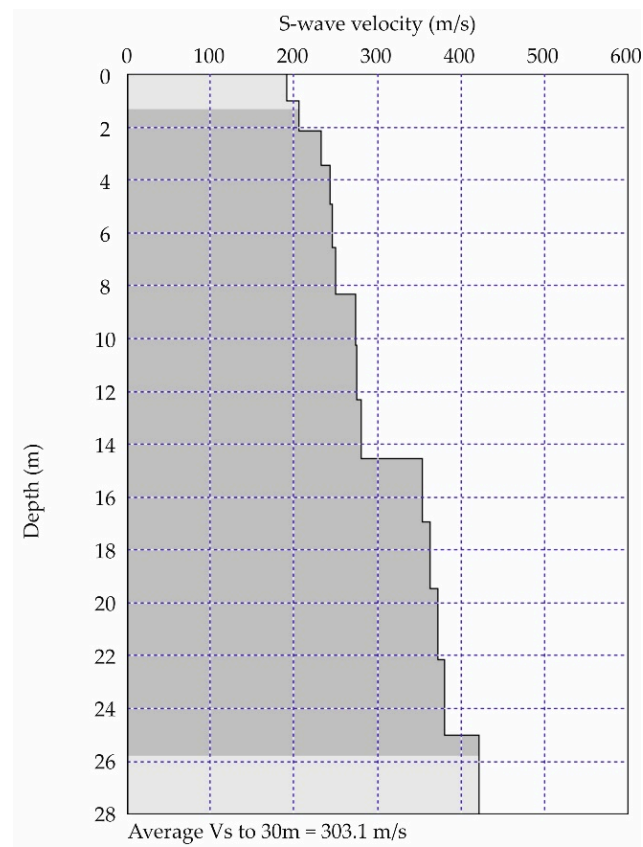


Figure A5. 1D Vs model derived from the MASW technique at THAL station.

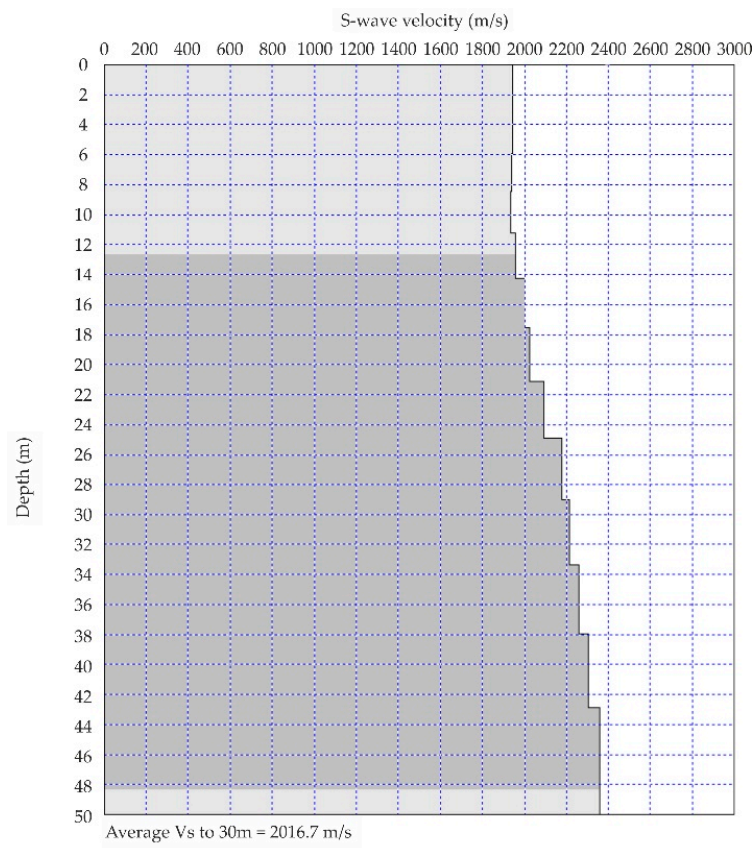


Figure A6. 1D Vs model derived from the MASW technique at ATAL station.

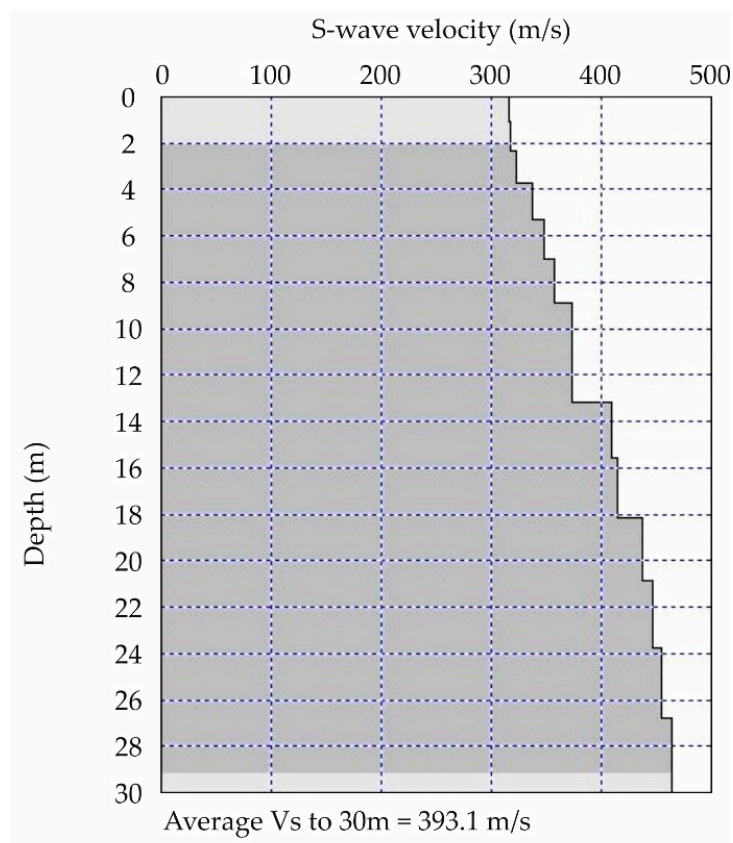


Figure A7. 1D Vs model derived from the MASW technique at EPID station.

## Appendix C

The results of the HVSR technique are summarized in Table A1, where all the peak frequencies and corresponding amplification factors are presented.

**Table A1.** Observed peak frequencies ( $f_i$ ) and associated amplification factors ( $A_i$ ). Values marked with an asterisk (\*) correspond to the dominant peak frequency,  $f_p$  (highest amplification). The adapted fundamental frequencies,  $f_0$ , (Table 5) are indicated in bold.

	$f_1$ (Hz)	$A_1$	$f_2$ (Hz)	$A_2$	$f_3$ (Hz)	$A_3$	$f_4$ (Hz)	$A_4$
MDRA	1.6 ± 0.1	1.4 ± 0.3	2.3 *	1.7 ± 0.3	2.7	1.7 ± 0.3		
VILL	1.2	1.8 ± 0.4	1.5	1.9 ± 0.4	<b>10.4 *</b>	1.9 ± 0.3		
LOUT	1.4	2.3 ± 0.5	2.5 ± 0.1	2.6 ± 0.1	<b>2.7 *</b>	3.1 ± 0.7	5.1 ± 0.1	2.2 ± 0.4
THAL	<b>1.4 *</b>	1.7 ± 0.4	2.3	1.6 ± 0.3				
ATAL	1.0 *	1.3 ± 0.3	13.6	1.2 ± 0.2				
EPID	1.5 ± 0.1	1.0 ± 0.3	4.1 ± 0.1	1.3 ± 0.5	6.5 ± 0.1	2.3 ± 0.8	<b>7.1 *</b>	2.6 ± 0.5

## References

- University of Athens. Hellenic Seismological Network, University of Athens, Seismological Laboratory [Data set]. International Federation of Digital Seismograph Networks. 2008. Available online: <https://www.fdsn.org/networks/detail/HA/> (accessed on 20 March 2023).
- Evangelidis, C.P.; Triantafyllis, N.; Samios, M.; Boukouras, K.; Kontakos, K.; Ktenidou, O.-J.; Fountoulakis, I.; Kalogeras, I.; Melis, N.S.; Galanis, O.; et al. Seismic Waveform Data from Greece and Cyprus: Integration, Archival, and Open Access. *Seismol. Res. Lett.* **2021**, *92*, 1672–1684. Available online: <https://pubs.geoscienceworld.org/ssa/srl/article-abstract/92/3/1672/595244/Seismic-Waveform-Data-from-Greece-and-Cyprus?redirectedFrom=fulltext> (accessed on 20 March 2023). [CrossRef]
- National Observatory of Athens, Institute of Geodynamics, Athens. National Observatory of Athens Seismic Network [Data Set]. International Federation of Digital Seismograph Networks. 1975. Available online: <https://www.fdsn.org/networks/detail/HL/> (accessed on 20 March 2023).
- Aristotle University of Thessaloniki. Aristotle University of Thessaloniki Seismological Network [Data Set]. International Federation of Digital Seismograph Networks. 1981. Available online: <https://www.fdsn.org/networks/detail/HT/> (accessed on 20 March 2023).
- University of Patras. University of Patras, Seismological Laboratory [Data Set]. International Federation of Digital Seismograph Networks. 2000. Available online: <https://www.fdsn.org/networks/detail/HP/> (accessed on 20 March 2023).
- Technological Educational Institute of Crete. Seismological Network of Crete [Data Set]. International Federation of Digital Seismograph Networks. 2006. Available online: <https://www.fdsn.org/networks/detail/HC/> (accessed on 20 March 2023).
- Institute of Engineering Seimology Earthquake Engineering. ITSAK Strong Motion Network [Data Set]. International Federation of Digital Seismograph Networks. 1981. Available online: <https://www.fdsn.org/networks/detail/HI/> (accessed on 20 March 2023).
- Rodriguez-Marek, A.; Rathje, E.M.; Bommer, J.J.; Scherbaum, F.; Stafford, P.J. Application of single-station sigma and site-response characterization in a probabilistic seismic-hazard analysis for a new nuclear site. *Bull. Seismol. Soc. Am.* **2014**, *104*, 1601–1619. [CrossRef]
- Bindi, D.; Cotton, F.; Kotha, S.R.; Bosse, C.; Stromeyer, D.; Grünthal, G. Application-driven ground motion prediction equation for seismic hazard assessments in non-cratonic moderate-seismicity areas. *J. Seismol.* **2017**, *21*, 1201–1218. [CrossRef]
- Bindi, D.; Parolai, S.; Gómez-Capera, A.; Locati, M.; Kalmetyeva, Z.; Mikhailova, N. Locations and magnitudes of earthquakes in Central Asia from seismic intensity data. *J. Seismol.* **2014**, *18*, 1–21. [CrossRef]
- Lanzano, G.; Luzi, L.; D'Amico, V.; Pacor, F.; Meletti, C.; Marzocchi, W.; Rotondi, R.; Varini, E. Ground motion models for the new seismic hazard model of Italy (MPS19): Selection for active shallow crustal regions and subduction zones. *Bull. Earthq. Eng.* **2020**, *18*, 3487–3516. [CrossRef]
- Priolo, E.; Pacor, F.; Spallarossa, D.; Milana, G.; Laurenzano, G.; Romano, M.A.; Felicetta, C.; Hailemichael, S.; Cara, F.; Di Giulio, G.; et al. Seismological analyses of the seismic microzonation of 138 municipalities damaged by the 2016–2017 seismic sequence in Central Italy. *Bull. Earthq. Eng.* **2020**, *18*, 5553–5593. [CrossRef]
- Al-Heety, A.J.; Hassouneh, M.; Abdullah, F.M. Application of MASW and ERT methods for geotechnical site characterization: A case study for roads construction and infrastructure assessment in Abu Dhabi, UAE. *J. Appl. Geophys.* **2021**, *193*, 104408. [CrossRef]
- Cardarelli, E.; Cercato, M.; De Donno, G. Characterization of an earth-filled dam through the combined use of electrical resistivity tomography, P-and SH-wave seismic tomography and surface wave data. *J. Appl. Geophys.* **2014**, *106*, 87–95. [CrossRef]
- Mohammed, M.A.; Abudeif, A.M.; Abd El-aal, A.K. Engineering geotechnical evaluation of soil for foundation purposes using shallow seismic refraction and MASW in 15th Mayo, Egypt. *J. Afr. Earth Sci.* **2020**, *162*, 103721. [CrossRef]

16. Pegah, E.; Liu, H. Application of near-surface seismic refraction tomography and multichannel analysis of surface waves for geotechnical site characterizations: A case study. *Eng. Geol.* **2016**, *208*, 100–113. [[CrossRef](#)]
17. Romero-Ruiz, A.; Linde, N.; Keller, T.; Or, D. A review of geophysical methods for soil structure characterization. *Rev. Geophys.* **2018**, *56*, 672–697. [[CrossRef](#)]
18. Salem, H.S. Poisson's ratio and the porosity of surface soils and shallow sediments, determined from seismic compressional and shear wave velocities. *Geotechnique* **2000**, *50*, 461–463. [[CrossRef](#)]
19. Cultrera, G.; Cornou, C.; Di Giulio, G.; Bard, P.Y. Indicators for site characterization at seismic station: Recommendation from a dedicated survey. *Bull. Earthq. Eng.* **2021**, *19*, 4171–4195. [[CrossRef](#)]
20. Macau, A.; Benjumea, B.; Gabàs, A.; Figueras, S. Optimal Application of Geophysical Techniques for Subsoil Characterization of Seismic Stations. In Proceedings of the Near Surface Geoscience 2015-21st European Meeting of Environmental and Engineering Geophysics, Turin, Italy, 6–10 September 2015; European Association of Geoscientists & Engineers: Utrecht, The Netherlands, 2015; Volume 1, pp. 1–5. [[CrossRef](#)]
21. Leyton, F.; Leopold, A.; Hurtado, G.; Pastén, C.; Ruiz, S.; Montalva, G.; Saéz, E. Geophysical characterization of the Chilean seismological stations: First results. *Seismol. Res. Lett.* **2018**, *89*, 519–525. [[CrossRef](#)]
22. Di Giulio, G.; Cultrera, G.; Cornou, C.; Bard, P.Y.; Al Tfaily, B. Quality assessment for site characterization at seismic stations. *Bull. Earthq. Eng.* **2021**, *19*, 4643–4691. [[CrossRef](#)]
23. Farrugia, J.J.; Molnar, S.; Atkinson, G.M. Noninvasive Techniques for Site Characterization of Alberta Seismic Stations Based on Shear-Wave Velocity. *Bull. Seismol. Soc. Am.* **2017**, *107*, 2885–2902. [[CrossRef](#)]
24. Nakamura, Y. A method for dynamic characteristics estimation of subsurface using microtremor on the ground surface. *Railw. Tech. Res. Inst. Q. Rep.* **1989**, *30*, 25–33.
25. Gorstein, M.; Ezersky, M. Combination of HVSR and MASW Methods to Obtain Shear Wave Velocity Model of Subsurface in Israel. *Int. J. Georesources Environ. -IJGE* **2015**, *1*, 20–41. [[CrossRef](#)]
26. Stanko, D.; Markušić, S.; Strelec, S.; Gazdek, M. HVSR Analysis of Seismic Site Effects and Soil-Structure Resonance in Varaždin City (North Croatia). *Soil Dyn. Earthq. Eng.* **2017**, *92*, 666–677. [[CrossRef](#)]
27. Fat-Helbary, R.E.-S.; El-Faragawy, K.O.; Hamed, A. Application of HVSR Technique in the Site Effects Estimation at the South of Marsa Alam City, Egypt. *J. Afr. Earth Sci.* **2019**, *154*, 89–100. [[CrossRef](#)]
28. Arimuko, A.; Santoso, E.; Sunardi, B. Investigation of Site Condition Using Elliptical Curve Inversion from Horizontal-to-Vertical Spectral Ratio (HVSR). *J. Phys. Conf. Ser.* **2020**, *1491*, 012031. [[CrossRef](#)]
29. Capizzi, P.; Martorana, R. Analysis of HVSR Data Using a Modified Centroid-Based Algorithm for Near-Surface Geological Reconstruction. *Geosciences* **2022**, *12*, 147. [[CrossRef](#)]
30. Napolitano, F.; Gervasi, A.; La Rocca, M.; Guerra, I.; Scarpa, R. Site effects in the pollino region from the HVSR and polarization of seismic noise and earthquakes site effects in the pollino region from the HVSR and polarization of seismic noise and earthquakes. *Bull. Seismol. Soc. Am.* **2018**, *108*, 309–321. [[CrossRef](#)]
31. La Rocca, M.; Chiappetta, G.D.; Gervasi, A.; Festa, R.L. Non-stability of the noise HVSR at sites near or on topographic heights. *Geophys. J. Int.* **2020**, *222*, 2162–2171. [[CrossRef](#)]
32. Kassaras, I.; Kalantoni, D.; Kouskouna, V.; Pomonis, A.; Michalaki, K.; Stoumpos, P.; Mourloukos, S.; Birmpilopoulos, S.; Makropoulos, K. Correlation between damage distribution and soil characteristics deduced from ambient vibrations in the old town of Lefkada (W Greece). In Proceedings of the 2nd European Conference on Earthquake Engineering and Seismology, Istanbul, Turkey, 25–29 August 2014. Paper n. 251.
33. Kassaras, I.; Papadimitriou, P.; Kapetanidis, V.; Voulgaris, N. Seismic Site Characterization at the Western Cephalonia Island in the Aftermath of the 2014 Earthquake Series. *Int. J. Geo-Eng.* **2017**, *8*, 1–22. [[CrossRef](#)]
34. Kassaras, I.; Kazantzidou-Firtinidou, D.; Ganas, A.; Kapetanidis, V.; Tsimi, C.; Valkaniotis, S.; Sakellariou, N.; Mourloukos, S. Seismic Risk and Loss Assessment for Kalamata (SW Peloponnese, Greece) from Neighbouring Shallow Sources. *Boll. Di Geofis. Teor. Ed Appl.* **2018**, *59*, 1–26. [[CrossRef](#)]
35. Theodoulidis, N.; Cultrera, G.; Cornou, C.; Bard, P.-Y.; Boxberger, T.; DiGiulio, G.; Imtiaz, A.; Kementzetzidou, D.; Makra, K.; The Argostoli NERA Team. Basin Effects on Ground Motion: The Case of a High-Resolution Experiment in Cephalonia (Greece). *Bull. Earthq. Eng.* **2018**, *16*, 529–560. [[CrossRef](#)]
36. Rigo, A.; Sokos, E.; Lefils, V.; Briole, P. Seasonal Variations in Amplitudes and Resonance Frequencies of the HVSR Amplification Peaks Linked to Groundwater. *Geophys. J. Int.* **2021**, *226*, 1–13. [[CrossRef](#)]
37. Adewoyin, O.O.; Joshua, E.O.; Akinyemi, M.L.; Omeje, M.; Adagunodo, T.A. Evaluation of geotechnical parameters of reclaimed land from near-surface seismic refraction method. *Heliyon* **2021**, *7*, e06765. [[CrossRef](#)]
38. Khalil, M.H.; Hanafy, S.M. Engineering applications of seismic refraction method: A field example at Wadi Wardan, Northeast Gulf of Suez, Sinai, Egypt. *J. Appl. Geophys.* **2008**, *65*, 132–141. [[CrossRef](#)]
39. Yilmaz, O.; Eser, M.; Berilgen, M. Seismic, geotechnical, and earthquake engineering site characterization. In *SEG Technical Program Expanded Abstracts*; Society of Exploration Geophysicists: Tulsa, OK, USA, 2006; pp. 1401–1405. [[CrossRef](#)]
40. Zhang, J.; Toksöz, M.N. Nonlinear refraction travelttime tomography. *Geophysics* **1998**, *63*, 1726–1737. [[CrossRef](#)]
41. Zhu, X.; Sixta, D.P.; Angstman, B.G. Tomostatics: Turning-ray tomography+ static corrections. *Lead. Edge* **1992**, *11*, 15–23. [[CrossRef](#)]
42. Stefani, J.P. Turning-ray tomography. *Geophysics* **1995**, *60*, 1917–1929. [[CrossRef](#)]

43. Lanz, E.; Maurer, H.; Green, A.G. Refraction tomography over a buried waste disposal site. *Geophysics* **1998**, *63*, 1414–1433. [[CrossRef](#)]
44. Thurber, C.; Ritsema, J. Theory and observations-seismic tomography and inverse methods. *Seismol. Struct. Earth* **2007**, *1*, 323–360. [[CrossRef](#)]
45. Foti, S.; Parolai, S.; Albarello, D.; Picozzi, M. Application of surface-wave methods for seismic site characterization. *Surv. Geophys.* **2011**, *32*, 777–825. [[CrossRef](#)]
46. Socco, L.V.; Strobbia, C. Surface-wave method for near-surface characterization: A tutorial. *Near Surf. Geophys.* **2004**, *2*, 165–185. [[CrossRef](#)]
47. Park, C.B.; Miller, R.D.; Xia, J. Multichannel analysis of surface waves. *Geophysics* **1999**, *64*, 800–808. [[CrossRef](#)]
48. Eker, A.M.; Akgün, H.; Koçkar, M.K. Local site characterization and seismic zonation study by utilizing active and passive surface wave methods: A case study for the northern side of Ankara, Turkey. *Eng. Geol.* **2012**, *151*, 64–81. [[CrossRef](#)]
49. Karlı, A.I.; Tildy, P.; Prónay, Z.; Pınar, A.; Hermann, L.  $V_S^{30}$  mapping and soil classification for seismic site effect evaluation in Dinar region, SW Turkey. *Geophys. J. Int.* **2006**, *165*, 223–235. [[CrossRef](#)]
50. Karabulut, S. Soil classification for seismic site effect using MASW and ReMi methods: A case study from western Anatolia (Dikili-İzmir). *J. Appl. Geophys.* **2018**, *150*, 254–266. [[CrossRef](#)]
51. Xia, J.; Miller, R.D.; Park, C.B.; Hunter, J.A.; Harris, J.B.; Ivanov, J. Comparing shear-wave velocity profiles inverted from multichannel surface wave with borehole measurements. *Soil Dyn. Earthq. Eng.* **2002**, *22*, 181–190. [[CrossRef](#)]
52. SESAME. Guidelines for Implementation of the H/V Spectral Ratio Technique on AMBIENT Vibrations: Measurements, Processing and Interpretation, European Commission–EVG1-CT-2000-00026 SESAME. 2004. Available online: [http://sesame.geopsy.org/Papers/HV\\_User\\_Guidelines.pdf](http://sesame.geopsy.org/Papers/HV_User_Guidelines.pdf) (accessed on 9 March 2023).
53. Allen, R.V. Automatic Earthquake Recognition and Timing from Single Traces. *Bull. Seismol. Soc. Am.* **1978**, *68*, 1521–1532. [[CrossRef](#)]
54. Konno, K.; Ohmachi, T. Ground-Motion Characteristics Estimated from Spectral Ratio between Horizontal and Vertical Components of Microtremor. *Bull. Seismol. Soc. Am.* **1998**, *88*, 228–241. [[CrossRef](#)]
55. Geometrics Inc.; OYO Inc. *SeisImager Manual Version 3.3 [Computer Program Manual]*; OYO Corporation: Tokyo, Japan, 2009.
56. Babuska, V.; Cara, M. *Seismic Anisotropy in the Earth*; Kluwer Academic Publishers: Boston, MA, USA, 1991.
57. *EN 1998-1*; Eurocode 8: Design of Structures for Earthquake Resistance. Part 1: General Rules, Seismic Actions and Rules for Buildings. European Committee for Standardization (CEN): Brussels, Belgium, 2004.
58. Alexopoulos, J.D.; Voulgaris, N.; Dilalos, S.; Gkosios, V.; Giannopoulos, I.K.; Mitsika, G.S.; Vassilakis, E.m.; Sakkas, V.; Kaviris, G. Near-Surface Geophysical Characterization of Lithologies in Corfu and Lefkada Towns (Ionian Islands, Greece). *Geosciences* **2022**, *12*, 446. [[CrossRef](#)]
59. Vasilatos, C.; Anastasatou, M.; Alexopoulos, J.; Vassilakis, E.; Dilalos, S.; Antonopoulou, S.; Petrakis, S.; Delipetrou, P.; Georghiou, K.; Stamatakis, M. Assessment of the Geo-Environmental Status of European Union Priority Habitat Type “Mediterranean Temporary Ponds” in Mt. Oiti, Greece. *Water* **2019**, *11*, 1627. [[CrossRef](#)]
60. Alexopoulos, J.D.; Dilalos, S.; Vassilakis, E. Adumbration of Amvrakia’s spring water pathways, based on detailed geophysical data (Kastraki-Meteora). *Adv. Res. Aquat. Environ.* **2011**, *2*, 105–112. [[CrossRef](#)]
61. Abzalov, M.Z. Measuring and modelling of dry bulk rock density for mineral resource estimation. *Appl. Earth Sci.* **2013**, *122*, 16–29. [[CrossRef](#)]
62. Dilalos, S. Application of Geophysical Technique to the Investigation of Tectonic Structures in Urban and Suburban Environments. A Case Study in Athens Basin. Ph.D. Thesis, National and Kapodistrian University of Athens, Athens, Greece, 2018. Available online: <http://hdl.handle.net/10442/hedi/48791> (accessed on 20 March 2023).
63. Dilalos, S.; Alexopoulos, J.D.; Lozios, S. New insights on Athens basin (Greece) subsurface geological and tectonic structure, derived from urban gravity measurements. *J. Appl. Geophys.* **2019**, *167*, 73–105. [[CrossRef](#)]
64. Dilalos, S.; Alexopoulos, J.D.; Vassilakis, E.; Poulos, S.E. Investigation of the structural control of a deltaic valley with geophysical methods. The case study of Pineios river delta (Thessaly, Greece). *J. Appl. Geophys.* **2022**, *202*, 104652. [[CrossRef](#)]
65. García-Pérez, T.; Marquardt, C.; Yáñez, G.; Cembrano, J.; Gomila, R.; Santibañez, I.; Maringue, J. Insights on the structural control of a Neogene forearc basin in Northern Chile: A geophysical approach. *Tectonophysics* **2018**, *736*, 1–14. [[CrossRef](#)]
66. Parasnis, D.S. A study of rock densities in the English Midlands. *Geophys. Suppl. Mon. Not. R. Astron. Soc.* **1952**, *6*, 252–271. [[CrossRef](#)]
67. Lee, C.S.; Cho, T.C.; Lee, S.B.; Won, K.S. A study of weathering characteristic of Baeknokdam trachyte in Jeju Island. *J. Eng. Geol.* **2007**, *17*, 235–251.
68. Dounas, A. *Geological Map of Greece, Sheet Erythrai, Scale 1:50.000*; Institute of Geological and Mineralogical of Greece: Athens, Greece, 1971.
69. Papadimitriou, P.; Kaviris, G.; Makropoulos, K. Evidence of shear wave splitting in the eastern Korinthian Gulf (Greece). *Phys. Earth Planet. Inter.* **1999**, *114*, 3–13. [[CrossRef](#)]
70. Kaviris, G. Study of Seismic Source Properties of the Eastern Gulf of Corinth. Ph.D. Thesis, Faculty of Geology, University of Athens, Athens, Greece, 2003.
71. Bornovas, J.; Lalechos, N.; Filippakis, N. *Geological Map of Greece, Sheet Korinthos, Scale 1:50.000*; Institute of Geological and Mineralogical of Greece: Athens, Greece, 1969.

72. Koutsouveli, A.; Mettos, A. *Geological Map of Greece, Sheet Xilokastron, Scale 1:50.000*; Institute of Geological and Mineralogical of Greece: Athens, Greece, 1983.
73. Maratos, G. *Geological Map of Greece, Sheet Atalanti, Scale 1:50.000*; Institute of Geological and Mineralogical of Greece: Athens, Greece, 1965.
74. Bannert, D. *Geological Map of Greece, Sheet Ligourion, Scale 1:50.000*; Institute of Geological and Mineralogical of Greece: Athens, Greece, 1972.
75. Basheer, A.A.; Salama, N.S. Application of ERT and SSR for geotechnical site characterization: A case study for resort assessment in New El Alamein City, Egypt. *NRIAG J. Astron. Geophys.* **2022**, *11*, 58–68. [[CrossRef](#)]
76. Fat-Helbary, R.E.S.; El-Faragawy, K.O.; Hamed, A. Soil geotechnical characteristics for seismic risk mitigation at the southern extension of Marsa Alam city, Egypt. *NRIAG J. Astron. Geophys.* **2019**, *8*, 1–14. [[CrossRef](#)]
77. Gkosios, V.; Alexopoulos, J.D.; Giannopoulos, I.K.; Mitsika, G.S.; Dilalos, S.; Barbaresos, I.; Voulgaris, N. Determination of the subsurface geological regime and geotechnical characteristics at the area of Goudi (Athens, Greece) derived from geophysical measurements. *Bulletin of the Geological Society of Greece, Special Publication GSG2022-062*. In *Proceedings of the 16th International Congress of the Geological Society of Greece, Patras, Greece, 17–19 October 2022*.
78. Giannopoulos, I.K.; Alexopoulos, J.D.; Dilalos, S.; Gkosios, V.; Mitsika, G.S.; Stamatakis, M.; Voulgaris, N. The geophysical identification of lateritic bauxite formation at Mandra area, Attiki (Greece). *Bulletin of the Geological Society of Greece, Special Publication No 10, GSG2022-026*. In *Proceedings of the 16th International Congress of the Geological Society of Greece, Patras, Greece, 17–19 October 2022*.
79. Mitsika, G.S.; Alexopoulos, J.D.; Giannopoulos, I.K.; Gkosios, V.; Dilalos, S.; Filis, C.; Vassilakis, E.m.; Kaviris, G.; Sakkas, V.; Voulgaris, N. Preliminary results of near-surface geophysical survey in Lefkada town (Greece). *Bulletin of the Geological Society of Greece, Special Publication No 10, GSG2022-031*. In *Proceedings of the 16th International Congress of the Geological Society of Greece, Patras, Greece, 17–19 October 2022*.
80. Adams, L.H. *Elastic Properties of Materials of the Earth's Crust*. In *Internal Construction of the Earth (Edited by Gutenberg)*; Dover Publications, Inc.: New York, NY, USA, 1951.
81. Toksöz, M.N.; Cheng, C.H.; Timur, A. Velocities of seismic waves in porous rocks. *Geophysics* **1976**, *41*, 621–645. [[CrossRef](#)]
82. Ibs-von Seht, M.; Wohlenberg, J. Microtremors measurement used to map thickness of soft soils sediments. *Bull. Seismol. Soc. Am.* **1999**, *89*, 250–259. [[CrossRef](#)]

**Disclaimer/Publisher's Note:** The statements, opinions and data contained in all publications are solely those of the individual author(s) and contributor(s) and not of MDPI and/or the editor(s). MDPI and/or the editor(s) disclaim responsibility for any injury to people or property resulting from any ideas, methods, instructions or products referred to in the content.